CERN-BE-2022-001

HL-LHC Experiment Data Quality Working Group

Summary Report

Working Group Members

X. Buffat, I. Efthymiopoulos, L. Medina, R. Tomás, J. Wenninger
(CERN A&T Sector)
S.M. Demers Konezny, K. Einsweiler, R. Hawkings, B. Giacobbe, W.Kozanecki, C. Ohm, B. Petersen, A. Polini, A. Sfyrla, S. Pagan Griso, J. Strandberg, T. Strebler
(ATLAS Collaboration)
S. Bhattacharya, D. Bloch, D.N. Taylor, D.C. Gotardo, A. Dabrowski, F. Hartmann, A. Mohammadi, S. Mukherjee, M. Narain, G. Ortona, G. Pasztor, A. Purochit, A. Savin, S. Sekmen, D. Stickland
(CMS Collaboration)
L. Dufour, E. Thomas, M.R.J. Williams
(LHCb Collaboration)

CERN-BE-2022-001
01/03/2022

Abstract

This report summarizes the results of the HL-LHC Experimental Data Quality Working Group (EDQ WG). This WG has mainly focused on studying the characteristics of the luminous region in the high-luminosity experiments for the HL-LHC proton run. In particular, the impact of the longitudinal density of collision events on the performance of the detectors for the baseline but also possible variant configurations of the HL-LHC was studied and reported here. The report includes the findings on other operational topics in HL-LHC assessed by the WG like the bunch-to-bunch fluctuations in the delivered luminosity, the use of non-colliding bunches and luminosity calibration aspects.

Geneva, Switzerland
March 29, 2022

Contents

1 Introduction

The HL-LHC EDQ WG started its work in 2016 with the aim of studying the impact of the event pile-up density on the performance of the detector and provide feedback to the project on ways to optimize the machine configuration and its operational settings. At that time various hardware options were still considered for the HL-LHC baseline [1] like: 200 MHz or 800 MHz RF systems, the use of wires for the long-range beam-beam compensation, extra cavities for crab kissing or even the total absence of crab cavities. Since then, the use of any extra RF system has been discarded, and the crab cavities were reduced from 4 per beam and per IP side to 2. With this reduction only a partial compensation of the crossing angle is possible, 380 μrad out of the 500 μrad, resulting in an average peak pile-up density of 0.79(1.2) events/mm for the nominal(ultimate) operational parameters.

This report summarizes the results and findings of the WG and is organized as follows: Section 2 presents the machine scenarios with the expected evolution of key parameters during the physics fill. Section 3 highlights results on the expected detector performance considering a range of pile-up densities corresponding to operation with and without crab cavities in the current HL-LHC baseline. Section 4 discusses the observed bunch-by-bunch fluctuations in the LHC Run 2 and the detector tolerance to this unwanted effect during HL-LHC operation. Finally, Sections 5 and 6 summarize the discussions and findings within the WG on the need for, and parameters of, non-colliding bunches, and the requirements and constraints arising from the luminosity calibration at HL-LHC. It is to be noted that during the course of finalizing this report a new HL-LHC operational scenario has been developed for Run 4 [2] that is not considered here.

2 HL-LHC operational Scenarios

The maximum instantaneous luminosity L_{inst} of the HL–LHC will be limited by the maximum event pile-up (PU) per bunch crossing μ, that the high luminosity experiments ATLAS and CMS, located at the Interaction Points (IP) 1 and 5 respectively, will be able to handle. After the upgrade they are expected to cope with values of at least 140 and up to 200 events per bunch crossing. These values correspond to instantaneous luminosities of approximately $5 \times 10^{34}\text{cm}^{-2}\text{s}^{-1}$ and $7.5 \times 10^{34}\text{cm}^{-2}\text{s}^{-1}$ [3]. The HL–LHC project [4] aims to achieve a 'virtual' peak luminosity that is considerably higher than the maximum imposed by the acceptable event pile-up rate, and to control the instantaneous luminosity by levelling to a lower value L_{lev} during the physics fill ('luminosity levelling') so that the luminosity production can be sustained over longer periods to maximize the inte-

grated luminosity. The luminosity evolution can be estimated taking into account the beam population (N_{beam}) reduction due to the collisions (the so called 'burn-off') in the number (n_{IP}) of collision points and the emittance changes from synchrotron radiation damping and Intra-Beam scattering (IBS). The instantaneous luminosity L_{inst} is given by:

$$L_{inst} = \frac{n_b N^2 f_{rev} \gamma}{4\pi\beta^* \varepsilon_n} R(\beta^*, \sigma_z, d_{bb}) \tag{1}$$

where n_b is the number of colliding bunches per beam, N is the bunch population, f_{rev} is the beam revolution frequency, γ is the relativistic gamma factor and assuming equal R.M.S. normalized emittances ε_n in collision for both beams and transverse planes. The Twiss beta function β^* at the IP determines, together with ε_n, the R.M.S. beam size $\sigma^* = \sqrt{\varepsilon_n \beta^* / \gamma}$ at the IP (assuming that the contribution to the beam size due to the dispersion and the momentum spread of the beam can be neglected). Table 1 shows the key beam parameters in collisions for two production modes of the LHC beam in the injectors: **standard** [1] and **BCMS** [2].

The relevant machine and performance parameters along the physics fill for the baseline scenarios with and without crab cavities are shown in Figs. 1 and 2 respectively. Besides the usual beam parameters like intensity, transverse emittance and bunch length, instantaneous and integrated luminosity, few parameters of particular interest for HL-LHC are included. Their definition is repeated below, details can be found in Ref. [5].

pile-up

representing the average number of events per bunch crossing:

$$\mu(t) = \frac{\sigma \mathcal{L}()}{f n_b}$$

pile-up density

describing the line distribution of the events along s:

$$\rho(s,t) = \frac{\sigma}{f n_b} \frac{\partial \mathcal{L}(s,t)}{\partial s}, \text{ with } \mu(t) = \int \rho(s,t)\, ds$$

[1] In the standard LHC beam production scheme, each injected bunc from the PS Booster (PSB) is triple split at low energy and then twice double split followed by adiabatic bunch rotation at top energy to produce 12 bunches at extraction. With 6 injected PSB bunches per PS cycle this scheme produces a train of 72 bunches for LHC

[2] In the Bunch Compression Merging and Splitting (BCMS) LHC beam production sheme, two PSB bunches injected into the PS are first merged, then triple-split at low energy and then twice double split at top energy to produce 12 bunches. With 8 PSB bunches injected per PS cycle, this scheme produces a bunch train of 48 bunches for LHC

Table 1: HL–LHC nominal parameters for 25 ns operation for two production modes of the LHC beam in the injectors: standard and BCMS [4].

Parameter	LHC (design)	HL–LHC (standard)	HL–LHC (BCMS)[#]
Beam energy in collision [TeV]	7	7	7
Particles per bunch, N [10^{11}]	1.15	2.2	2.2
Number of bunches per beam	2808	2760	2744
Number of colliding bunches in IP1 and IP5*	2808	2748	2736
Total beam population N_{tot} [10^{14}]	3.2	6.1	6.0
Beam current [A]	0.58	1.10	1.10
Half-crossing angle in IP1 and IP5 [μrad]	142.5	250	250
Norm. beam–beam long–range sep. [σ]	9.4	10.5	10.5
Minimum β^* [m]	0.55	0.15	0.15
ε_n [μm]	3.75	2.50	2.50
Longitudinal emittance ε_L [eVs]	2.50	3.03	3.03
R.M.S. energy spread [10^{-4}] (q-Gaussian distr.)	-	1.1	1.1
R.M.S. energy spread [10^{-4}] (FWHM equiv. Gaussian)	1.13	1.29	1.29
R.M.S. bunch length [cm] (q–Gaussian distr.)	-	7.61	7.61
R.M.S. bunch length [cm] (FWHM equiv. Gaussian)	7.55	9.0	9.0
IBS horizontal [h]	105	16.5	16.5
IBS longitudinal [h]	63	19.2	19.2
Radiation damping [h]	26	26	26
Piwinski parameter	0.65	2.66	2.66
Total reduction factor R_0 w/o crab cav. at min. β^*	0.836	0.342	0.342
Total reduction factor R_1 w. crab cav. at min. β^*	-	0.716	0.716
Peak lumi. without crab cav. L_{peak} [10^{34} cm^{-2}s^{-1}]	1.00	8.11	8.07
Peak lumi. w. crab cav. L_{virt} [10^{34} cm^{-2}s^{-1}]	-	17.0	16.9
Events/crossing w/o levelling and w/o crab cav.	27	212	212
Levelled luminosity [10^{34} cm^{-2}s^{-1}]	-	5.0	5.0
Events/crossing μ (with levelling and crab cav.)[‡]	27	131	132
Max. line density of pile–up events [evts/mm]	0.21	1.3	1.3
Levelling time [h] (assuming no emittance growth)‡	-	7.2	7.2
Number of collisions in IP2	2808	2492	2246
IP8[**]	2808	2574	2370

[#] BCMS parameters are only considered for injection and as a backup parameter set in case one encounters larger–than–expected emittance growth in HL–LHC during injection, ramp, and squeeze.

[*] Assuming one less batch from the PS for machine protection (pilot injection, transfer line steering with 12 nominal bunches) and non-colliding bunches for experiments (background studies, etc.). Note that due to RF beam loading the abort gap length must not exceed the 3 μs design value.

[‡] The total number of events/crossing is calculated with an inelastic cross–section of 81 mb, while 111 mb is assumed as a pessimistic value for calculating the proton burn off and the resulting levelling time [3].

[**] The lower number of collisions in IR2/8 compared to the general-purpose detectors is a result of the agreed filling scheme, aiming as much as possible at an equal sharing of collisions between the experiments.

peak pile-up density

describing the maximum of the pile-up density $\rho(s,t)$ that is usually located at the interaction center (IP):

$$\hat{\rho}(t) = \rho(s=0,t)$$

effective pile-up density

calculated as the average of the pile-up density $\rho(s,t)$ over the duration of the collisions:

$$\overline{\rho} = \frac{\int_0^{t_{fill}} \int \rho^2 \, ds \, dt}{\int_0^{t_{fill}} \mu(t) \, dt}$$

The numerical simulations of the evolution of the beam parameters along the fill are described in [5], neglecting emittance growth from elastic scattering, from luminosity burn-off [6] and from potential power converter or crab cavity RF noise.

The LHCb performance luminosity evolution is shown in Fig. 3 for the baseline scenarios and the LHCb Phase II upgrade, where levelled luminosity is increased to 1.5×10^{34} cm^{-2}s^{-1}. It is shown that this upgrade reduces the integrated luminosity in ATLAS and CMS by 2%.

Table 2 summarizes the operational conditions, intensity adn luminosity ramp-up for the whole duration of the HL-LHC Run 4 and Run 5.

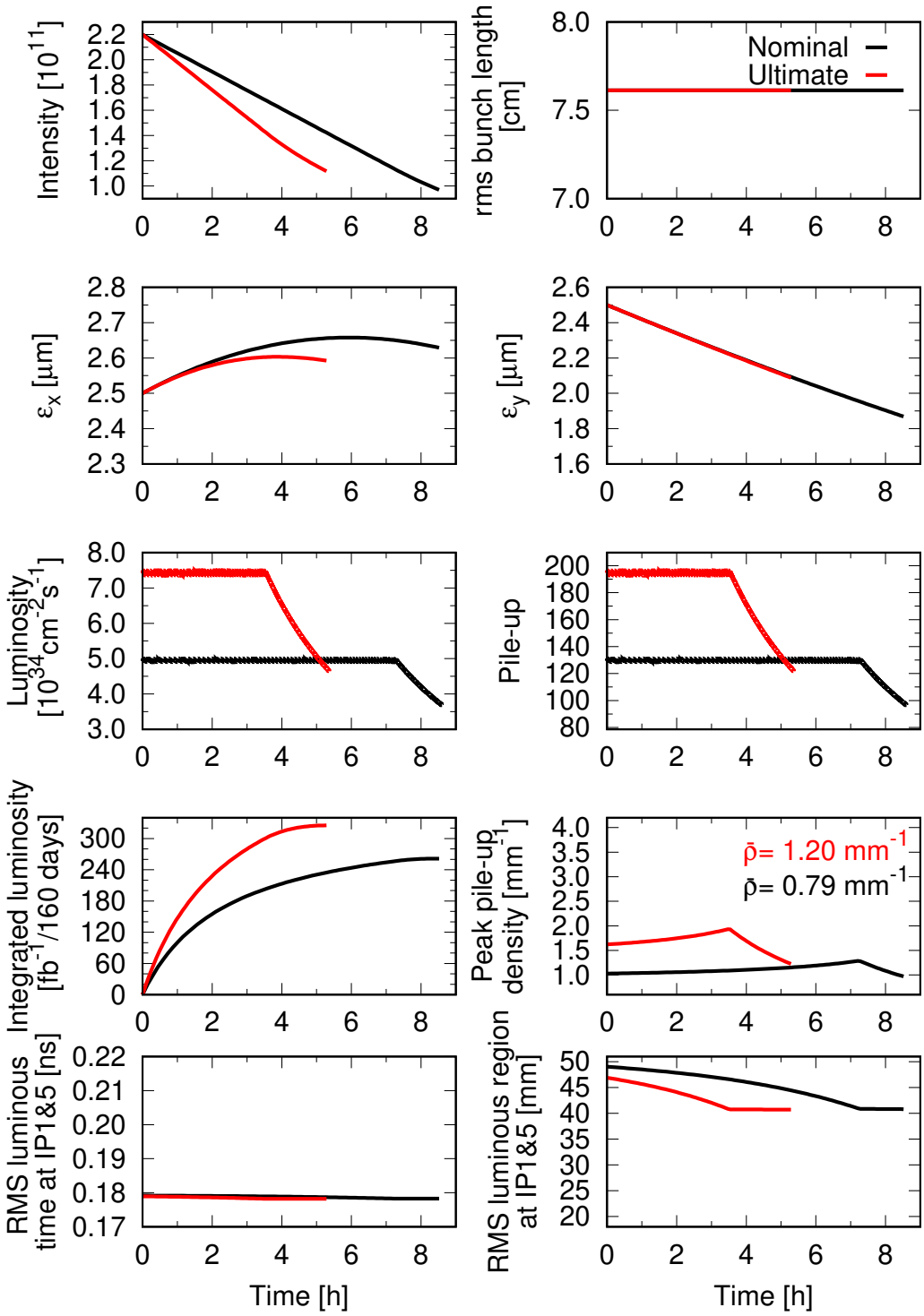

Figure 1: HL-LHC nominal and ultimate physics fills.

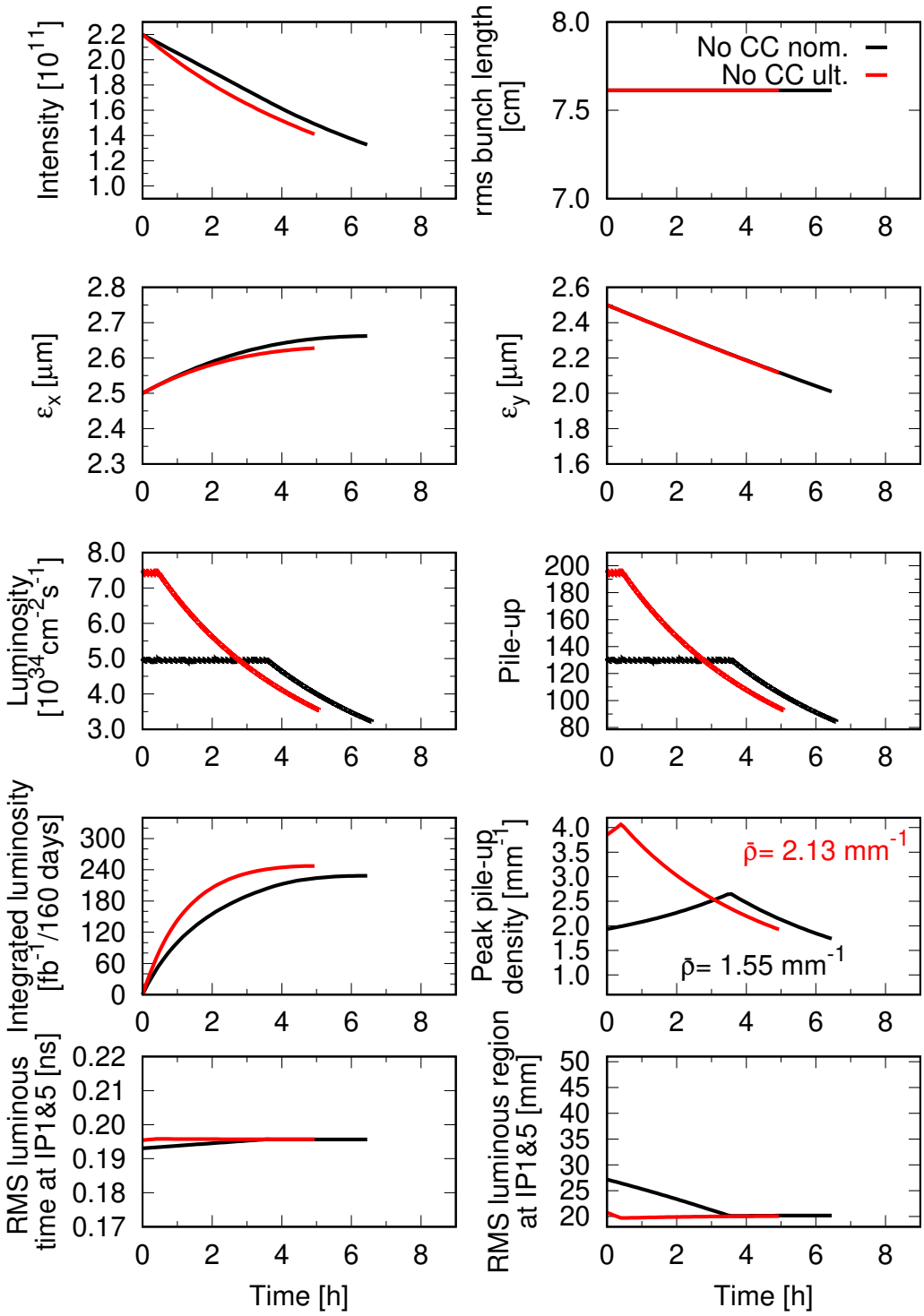

Figure 2: Physics fills without crab cavities for nominal and ultimate scenarios.

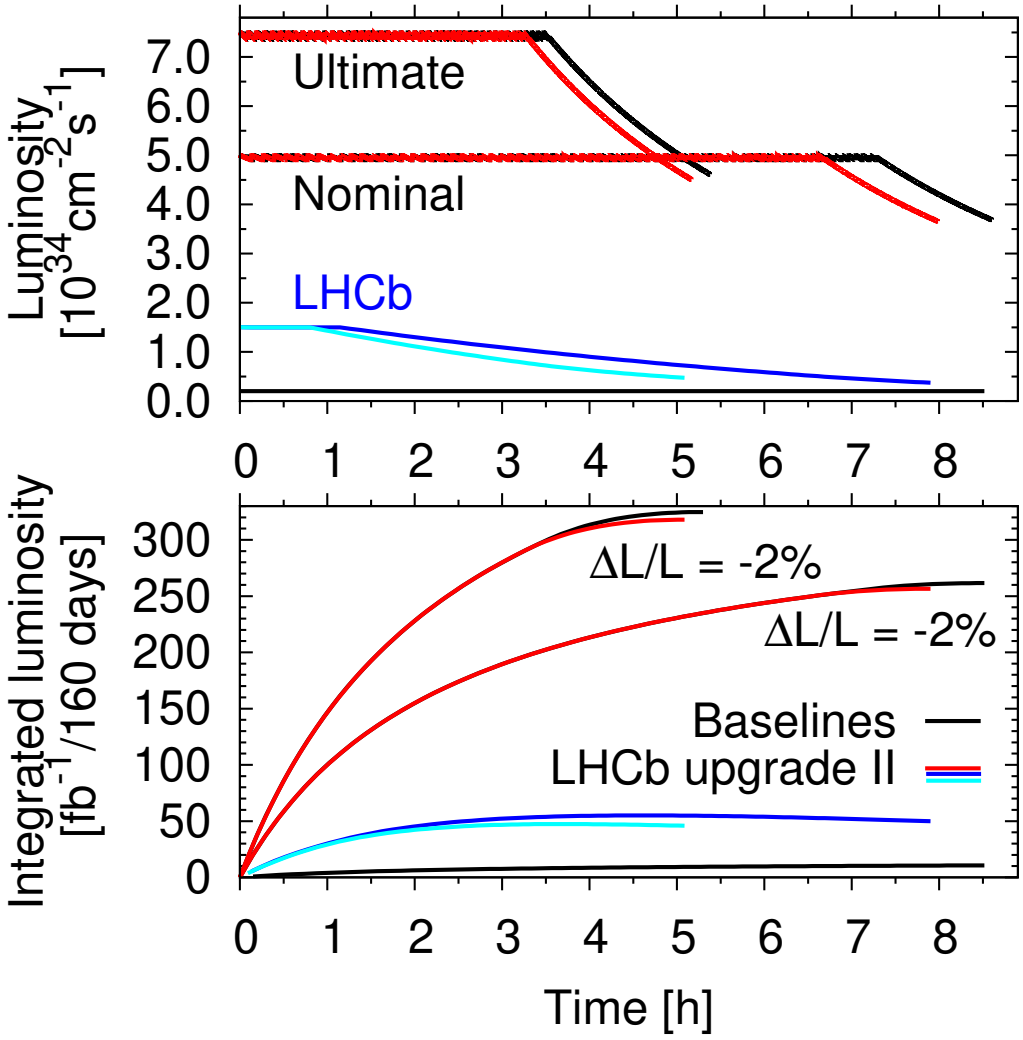

Figure 3: Physics fills for nominal and ultimate scenarios including the LHCb upgrade II. Black curves represent nominal and ultimate baseline scenarios, while colored curves correspond to the LHCb upgrade II.

Table 2: Protons per bunch (ppb), virtual luminosity (calculated with $\beta^* = \beta^*_{\text{end}}$), full crossing angle ($\theta$) and β^* targets in the HL-LHC luminosity ramp-up years[1]. A normalized emittance of $\varepsilon_n = 2.5$ μm is assumed for all years. β^*_{start} and β^*_{end} correspond to the IP β-function at the start and at the end of the physics fill. β^*_{start} is defined to deliver 2.5×10^{34} cm^{-2}s^{-1} at the start of the fill to meet requests from cryogenics. $\overline{\rho}$ is the effective pile-up density averaged over the collision adjustment process and along the physics fill [5]. The ultimate scenario is highlighted in yellow.

Year	ppb [10^{11}]	Virtual lumi. [10^{34}cm^{-2}s^{-1}]	Days in physics	θ [μrad]	β^*_{start} [cm]	β^*_{end} [cm]	HEL[#] & crab cav.	$\overline{\rho}$ [mm^{-1}]	Max. PU
2027	1.7	3.95	30	380	58	30	exp	0.69	104
2028	1.7	3.95	120	380	58	30	exp	0.69	104
2029	2.2	10.3	140	500	100	25	on	0.76	132
2030	2.2	13.5	160	500	100	20	on	0.78	132
2031	Long shutdown 4								
2032	2.2	13.5	170	500	100	20	on	0.78	132
2033	2.2	16.9	200	500	100	15	on	0.80	132
2033	2.2	16.9	200	500	100	15	on	1.20	200

[#] Hollow Electron Lenses, are devices designed to improve the cleaning efficiency of the collimation system by actively controlling the halo depletion speed for amplitude of betatron motion below the aperture restriction of the primary collimators.

[1] At the end of 2021 a re-scheduling of LHC and HL-LHC project took place. In the updated schedule the start of Run 4 is expected by 2029.

3 Impact of Pile-up and Pile-up Density on Experiment Performance

The higher pile-up and pile-up density of HL-LHC presents a significant challenge to most of the LHC experiments. In view of this ATLAS and CMS are preparing major detector upgrades for Run 4, while LHCb is studying upgrades for Run 5 to increase the instantaneous luminosity that can be handled. In this section the planned upgrades for ATLAS and CMS are briefly summarized, followed by studies on the impact of pile-up and pile-up density after the detector upgrades on lower-level tracking and vertexing, higher-level event reconstruction and some example HL-LHC physics channels. At the end some considerations for LHCb are given.

3.1 ATLAS and CMS HL-LHC upgrades

Both ATLAS and CMS experiments are planning significant upgrades of their detectors, the so-called Phase-2 upgrades, which will primarily take place during long shutdown 3, just before Run 4. For both experiments the tracker will be completely replaced with more radiation hard and higher granularity tracking sensors that can also provide efficient tracking up to pseudorapidities of about $|\eta| = 4$, where η is defined as

$$\eta = -\ln(\tan(\theta/2))) \tag{2}$$

and θ is the angle with respect to the beam axis. Most of the detector readout and trigger electronics will be replaced to provide higher granularity trigger inputs, higher trigger rate capability, and enable more advanced algorithms in order to maintain or improve on the trigger thresholds for all physics objects [3]. New muon detectors will be installed to either increase the geometrical coverage of the system up to $|\eta| = 2.8$ (CMS) or increase the system acceptance and redundancy (ATLAS). In CMS, the endcap electromagnetic and hadron calorimeters will be replaced with a new combined sampling calorimeter (HGCal) that should significantly improve reconstruction of particles in the endcap forward/backward regions. A new timing detector for minimum ionizing particles (MTD) in CMS for both barrel and endcap regions is envisaged to provide the capability for 4-dimensional reconstruction of interaction vertices. In ATLAS a High-Granularity Timing Detector (HGTD) is planned to provide pile-up mitigation for tracking in the forward region $2.8 < |\eta| < 4$.

[3] physics objects refer to reconstructed quantities that can be jets, identified charged or neutral particles, energy flow or higher-level combination of those.

A detailed overview of the CMS detector upgrade program is presented in Refs. [7, 8, 9, 10, 11, 12], while the expected performance of the reconstruction algorithms and pile-up mitigation with the CMS detector is summarised in Ref. [13, 14]. The detailed overview of the ATLAS upgrades are presented in Refs. [15, 16, 17, 18, 19, 20] and the expected performance under different pile-up conditions are presented in Ref. [21].

3.2 Tracking and vertexing performance

Tracking is one of the most important parts in the particle reconstruction, since it is used in most of the objects. Tracks can be used to associate reconstructed objects to different collision interactions and is thus the primary tool for mitigating pile-up and pile-up density effects.

Thanks to the upgraded tracking detectors with improved granularity and precision, the tracking performance is very robust against pile-up. This is illustrated in Fig. 4, which shows the inclusive track reconstruction efficiency in simulated $\sqrt{s} = 14\,\text{TeV}$ $t\bar{t}$ events. It is essentially constant as a function of pile-up (left plot). It also shows that the ratio of the number of reconstructed tracks to the number of generated charged particles as a function of pile-up is constant, indicating that increased pile-up does not visibly increase the number of fake tracks.

In addition to the track reconstruction, the assignation of the reconstructed tracks to vertex candidates, and the identification of the hard-scatter vertex candidate amongst all reconstructed vertices, are both important for ensuring effective pile-up mitigation for high-level physics objects. Figure 5 shows that at higher pile-up density, the number of reconstructed vertices decreases as vertices are merged. For $t\bar{t}$, a process with significant transverse activity, the efficiency of reconstructing the primary $t\bar{t}$ vertex remains close to 100% dropping by less than 1% at the highest pile-up density.

Assigning tracks to the correct primary vertex (PV) becomes more challenging as the pile-up density increases. This is illustrated in Fig. 6 where the number of pile-up (PU) tracks incorrectly associated with the primary vertex is seen to increase linearly with the PU density, independently of the total pile-up. This will affect the performance of physics objects that rely on assigning the correct vertex. In the case of CMS, this effect is reduced by the use of MTD precision timing as shown in Figure 6

3.3 Physics object performance

High levels of PU and high PU densities give rise to challenging experimental conditions, but as seen above, they do not significantly affect track and vertex reconstruction. This section contains studies on the impact of these challeng-

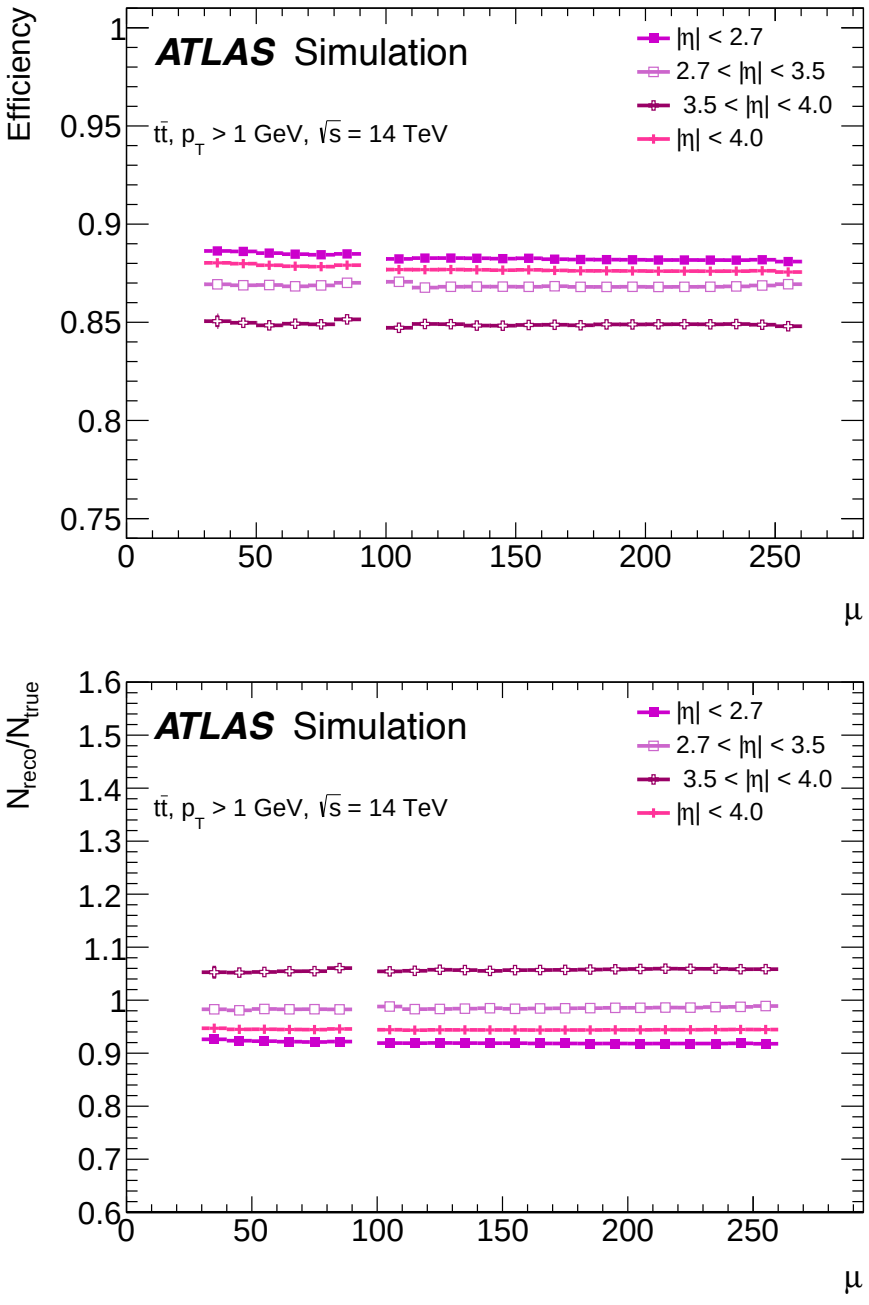

Figure 4: Top: Track reconstruction efficiency for $t\bar{t}$ events as a function of $\langle\mu\rangle$. Bottom: number of reconstructed tracks divided by the number of generated charged particles, for $t\bar{t}$ events. Figures taken from Ref. [16].

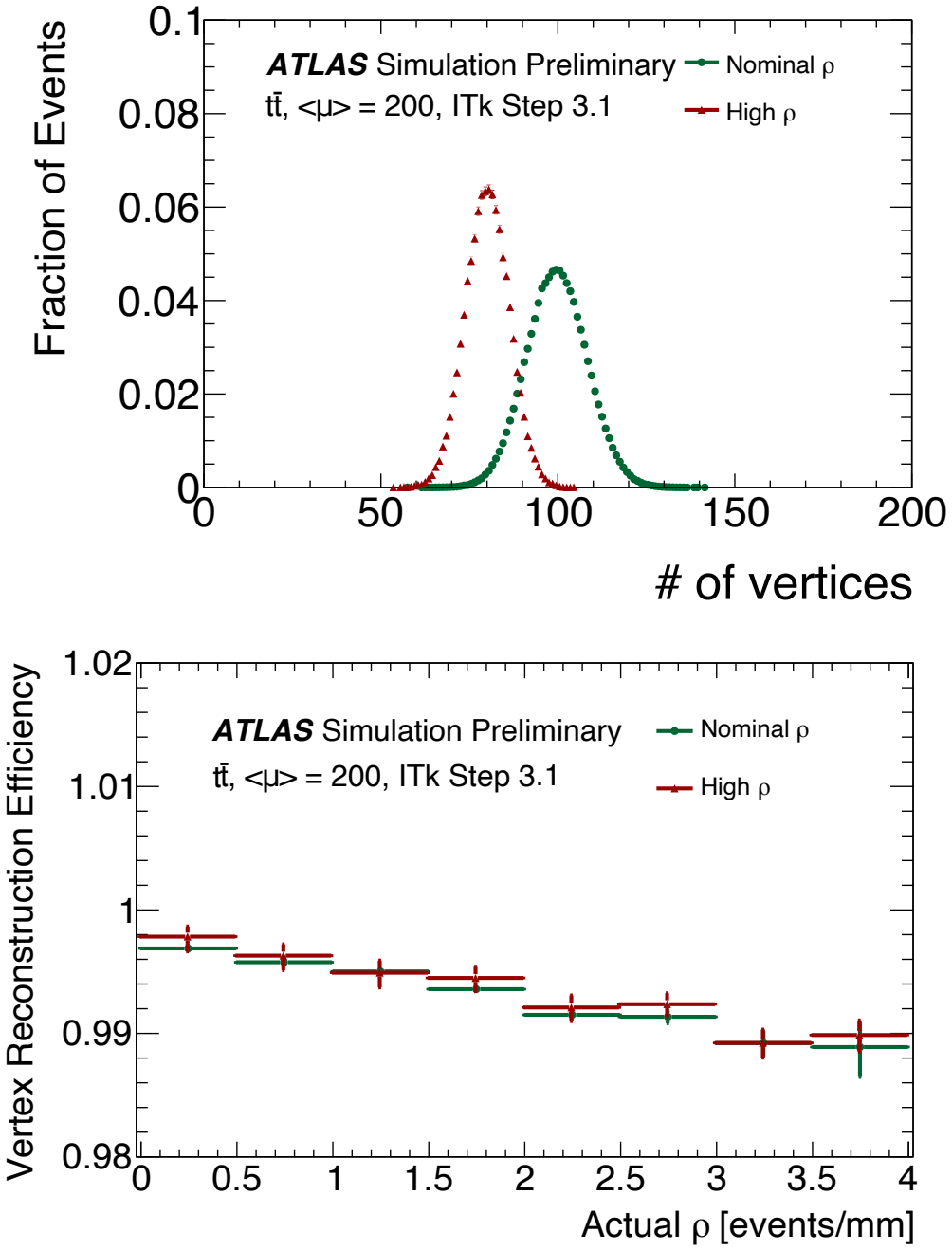

Figure 5: Top: Number of reconstructed vertices for $t\bar{t}$ events. Bottom: Vertex reconstruction efficiency as a function of the local pile-up density, for $t\bar{t}$ events. Taken from Ref. [21].

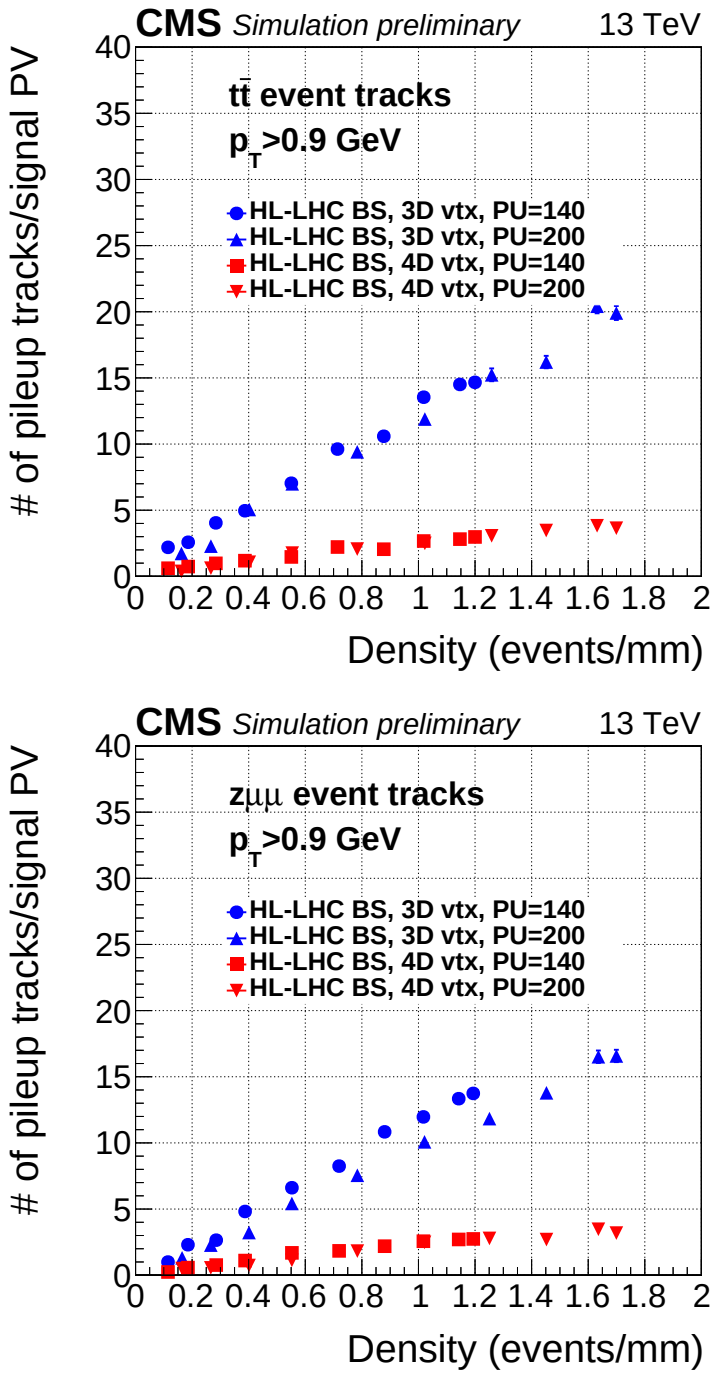

Figure 6: The number of PU tracks incorrectly associated with the primary vertex in $t\bar{t}$ (Left) and $Z \to \mu\mu$ (Right) events as a function of the PU density, shown with (4D vertex) and without (3D vertex) the MTD precision timing. Taken from Ref. [22].

ing conditions on the object reconstruction performance, where track and vertex requirements are combined with selections based on quantities measured in the calorimeters, muon system and timing detectors. These high-level objects (photons, leptons and jets) are directly used in physics analyses and any performance degradation affects the physics analysis performance. The impact is observed to be more significant than in pure tracking and vertexing studies.

The reconstruction efficiency of some objects will depend on the overall PU level as higher occupancy in for instance the calorimeter or muon detectors will start to affect the reconstruction algorithms if the sub-detector granularity is not high enough for objects to be well-separated. This can be seen for ATLAS in Fig. 7, where the reconstruction efficiency for electrons and muons drops by about 1% and 0.5%, respectively, when the PU is increased from 140 to 200. The right hand plot shows that this is not due to the higher PU density, but the overall PU level.

The efficiency of object identification is also expected to degrade with PU density. One of the reasons for this is that the isolation of objects, that is calculated in a cone around the leading particles is based mainly on the tracks of charged particles. Only particles associated with the primary vertex should be considered. With increased PU density, as discussed in the previous section, it becomes more difficult to separate particles from PU and primary vertexes. Therefore the amount of energy in the isolation cone increases as a function of PU density and the efficiency decreases as shown in the upper left plot of Fig. 8 for photon reconstruction. The sets of data points with linear fits represent different working points of the photon reconstruction and identification algorithm. The inverse is true for jets. Since the energy in the isolation cone increases, the misidentification probability of jets decreases with PU density as presented in the upper right plot of Fig. 8. For physics analyses it is usually essential to adjust the threshold for particle reconstruction such that the misidentification rate remains independent of PU density, since this is what defines the background contribution to the analysis, which is very difficult to simulate exactly in Monte Carlo, or estimate in other ways. Figure 8 shows the signal efficiency as a function of PU density for fixed misidentification probability. The linear fits to the data points demonstrate a very small negative slopes at around 0.5% per unit of PU density.

A similar effect of PU density on isolation efficiency is seen for charged leptons as illustrated in Fig. 9 for muons. The size of the effect will depend on the chosen efficiency working point and details of the selection algorithm as illustrated by the difference between the CMS and ATLAS results. In the CMS case an efficiency drop of about 2% per unit PU density is observed over the full rapidity range, whereas in ATLAS the selection was further optimized for the central region, reducing the efficiency drop to about 0.5% per unit PU density, while for forward muons there is a 3% efficiency loss. For hadronically decaying tau

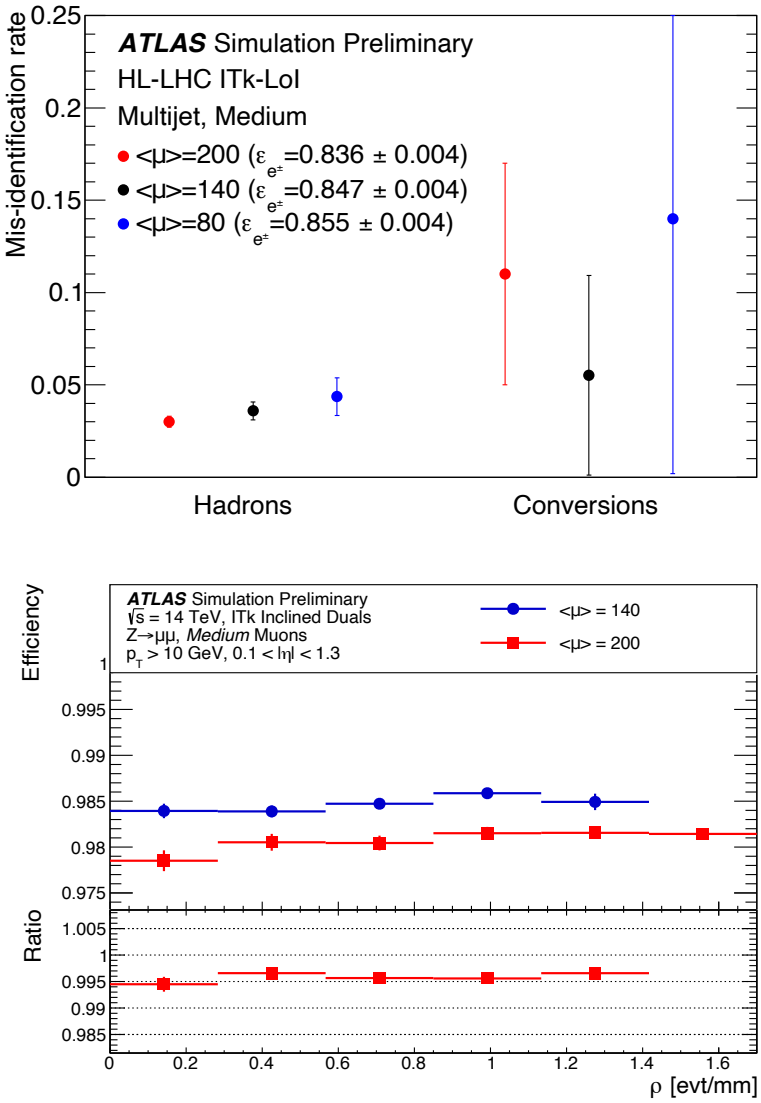

Figure 7: Top: The probability to mis-identify hadrons or photon conversions as electrons estimated using simulated multijet samples is given at different PU levels. The efficiencies for isolated electrons quoted in the legend ($\varepsilon_{e^{\pm}}$) were estimated using $Z \to ee$ decays. In all cases electron candidates are required to have $p_{\mathrm{T}} > 7\,\mathrm{GeV}$ and $|\eta| < 2.45$. Bottom: Muon reconstruction and identification efficiency for simulated $\sqrt{s} = 14\,\mathrm{TeV}$ $Z \to \mu\mu$ events at $\langle\mu\rangle$=140 (blue) / 200 (red), as a function of the the local PU density. Taken from Ref. [21].

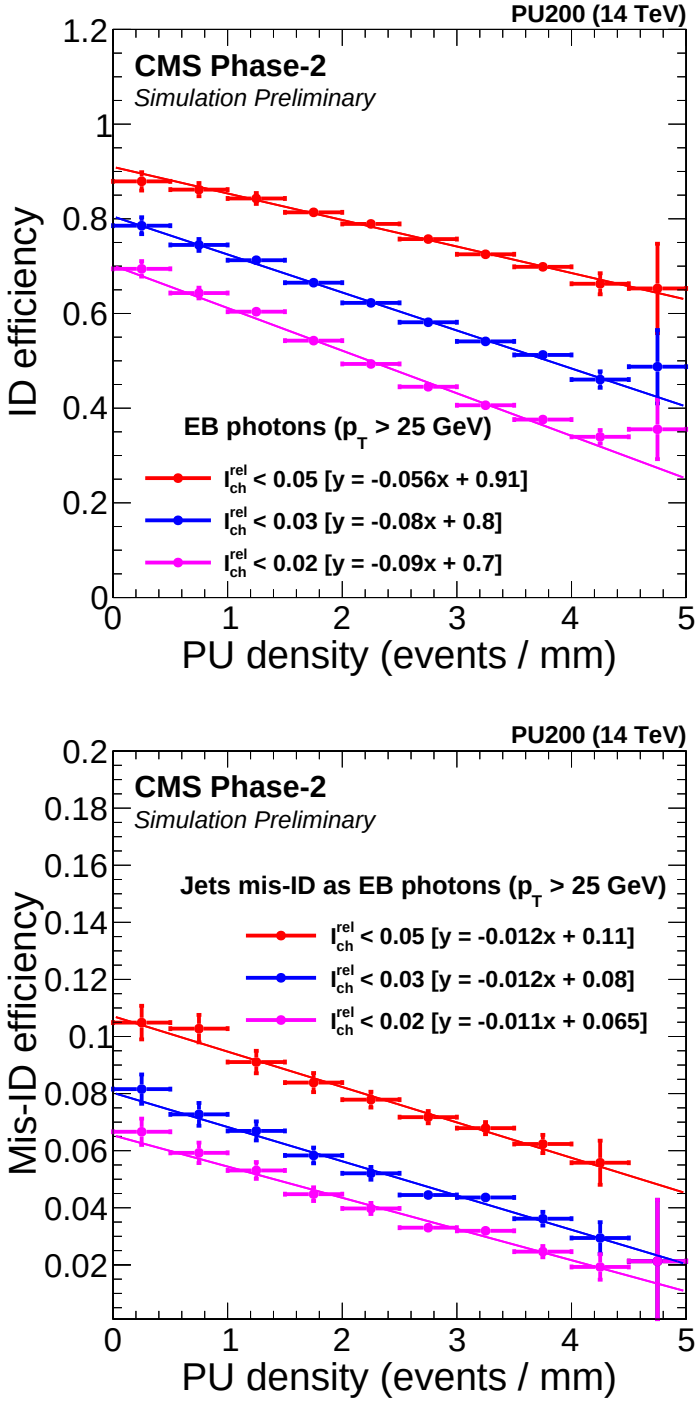

Figure 8: The photon efficiency (upper plot) and misidentification probability (bottom plot) for QCD jets to be reconstructed as photons for three working points of the photon reconstruction and identification algorithm.

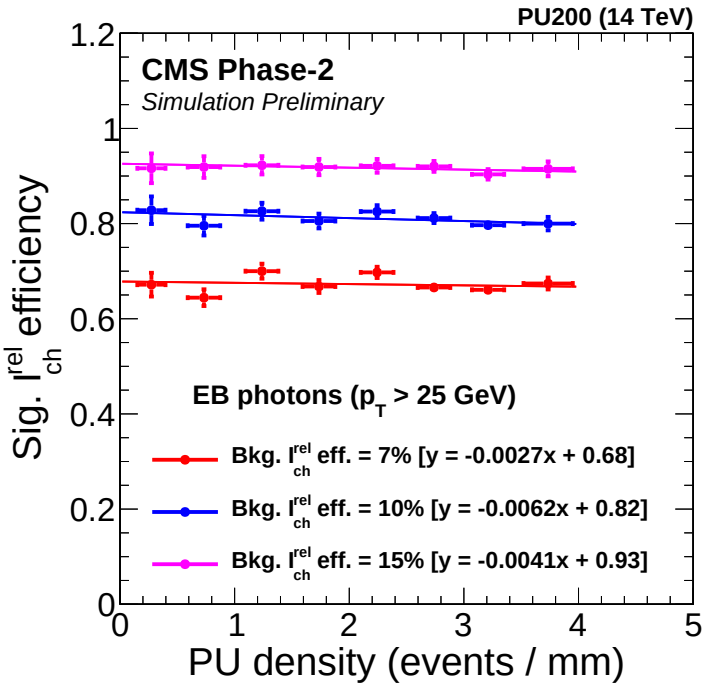

Figure 8: Photon efficiency for fixed misidentification probability [14].

leptons, isolation is even more critical to identify tau decays into 1 or 3 charged hadrons. A similar efficiency loss to the muon case is seen in Fig.10, which shows about a 1.5% drop in efficiency per unit PU density for a fixed background rate in CMS. A similar performance drop was observed in ATLAS studies.

Besides photons and leptons, jets are the other major physics object used in most physics analyses at ATLAS and CMS. Jets are reconstructed offline from Particle Flow (PF) objects (CMS) or topological clusters (ATLAS) and clustered using the anti-k_T algorithm [23, 24] with a distance parameter of 0.4. In CMS, see Ref. [25], various techniques for suppression of the PU contribution to jets can be applied: "Charged particles suppression" (CHPS) can be used based on association of particles in jets to the primary vertex. Or "pile-up per particle identification" (PUPPI). Figure 11 Left shows the corrected jet response resolution as a function of the PU density for jets corrected using different techniques. The resolution significantly improves when PU is specially treated but a small degradation in the jet energy resolution is observed as a function of the PU density.

In ATLAS, relatively simple pile-up suppression mechanisms have been studied so far for HL-LHC. For example the use of the R_{p_T} jet variable [26] was considered to select jets more likely to come from a primary vertex, where R_{p_T} is defined as the scalar sum of the p_T of all tracks that are inside the jet cone and

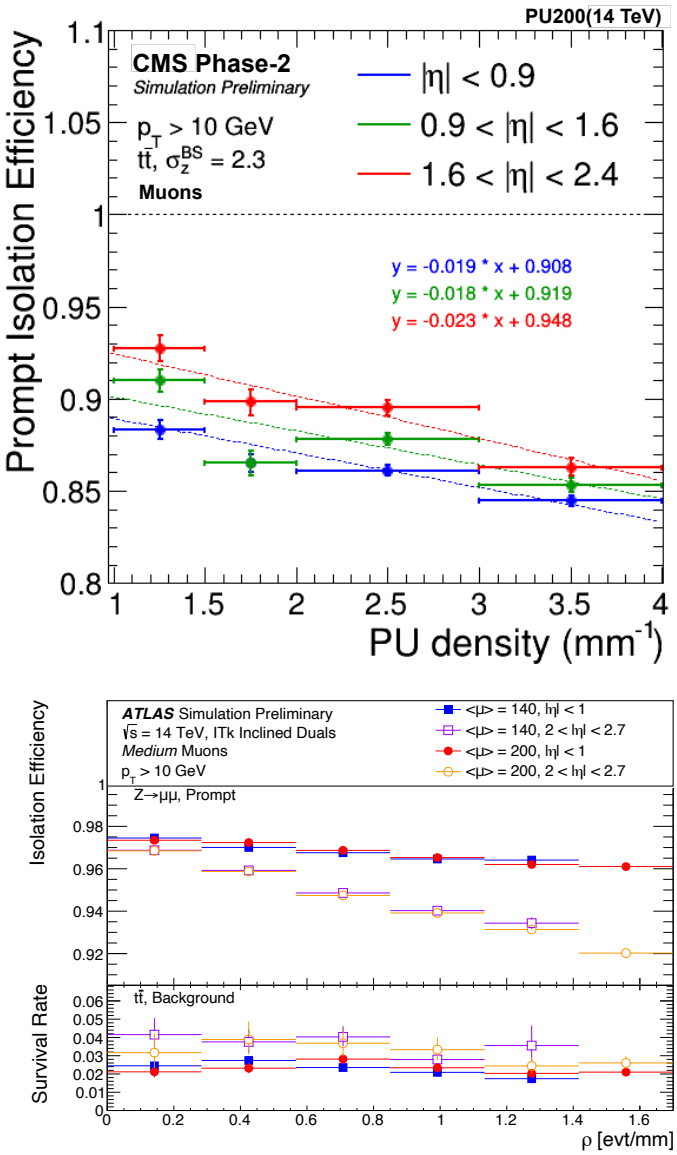

Figure 9: Muon isolation efficiency as a function of PU density for fixed misidentification probability for different regions of pseudorapidity in CMS (top) [14] and ATLAS (bottom) [21].

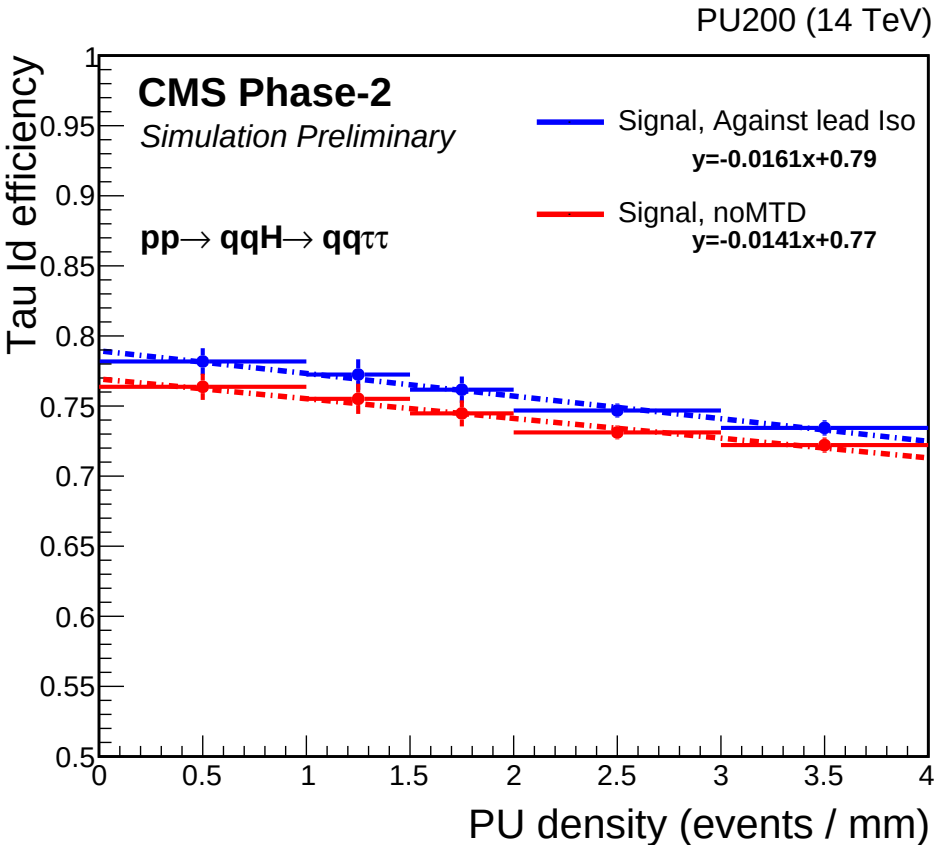

Figure 10: The efficiency of tau identification, including isolation as a function of PU density at fixed misidentification probability [14].

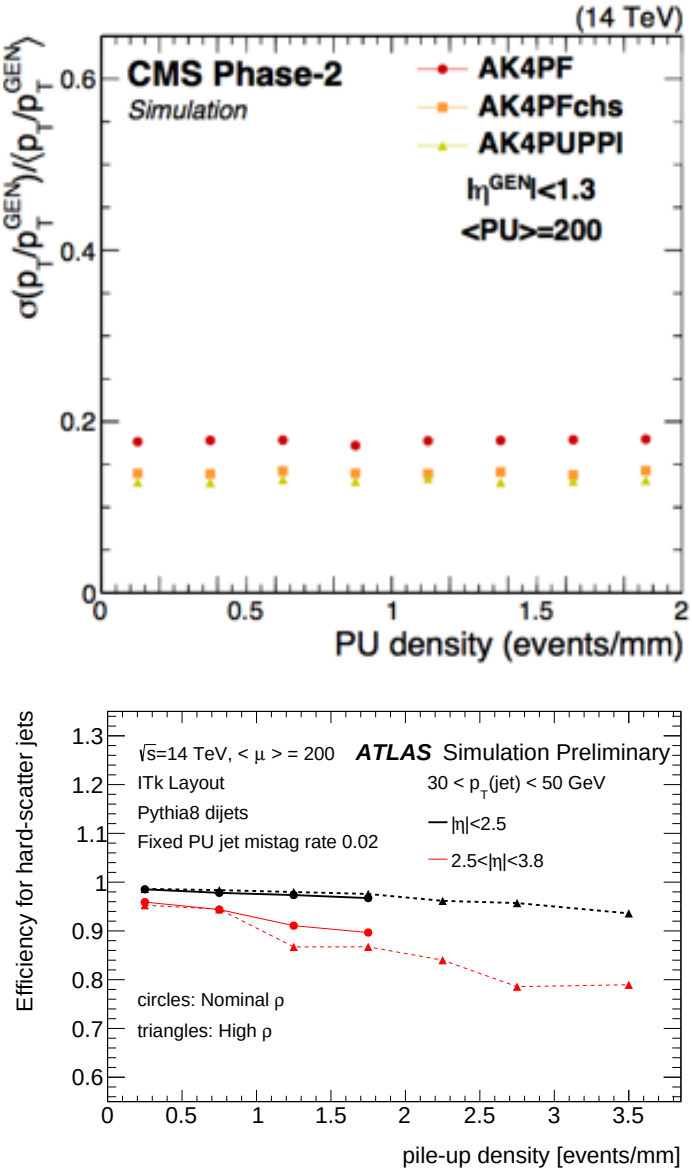

Figure 11: The corrected jet response resolution for $|\eta|< 1.3$ (top) as a function of the PU density for different jet algorithms with 200 PU. The jet algorithms shown are PF jets, PF jets with charged hadron subtraction, and PUPPI jets. All jets have been matched to a particle-level jet with 90 GeV $< p_{\mathrm{T}}^{\mathrm{Gen}} <$ 120 GeV. Taken from Ref. [25]. Efficiency for keeping hard-scatter jets, for $|\eta|< 2.5$ and $2.5 < |\eta|< 3.8$ (bottom), as a function of pile-up density measured in events with nominal (circles) and high pile-up density (triangles). Taken from Ref. [21].

originate from the selected primary vertex, divided by the jet p_{T}. As shown in Fig. 11 Right, a very large pile-up jet rejection (factor 50) can be achieved at the cost of some efficiency loss, particularly in the far forward region, and with a significant PU density dependence. Roughly 1.5% signal efficiency is lost per unit PU density in the central detector, while about a 4% drop is observed in the forward region. The use of precision timing from HGTD has not yet been included in this study, but is expected to improve the performance in the forward region.

The missing transverse momentum vector is an essential variable used in many physics analyses. It is defined as the projection onto the plane perpendicular to the beam axis of the negative vector sum [4] of the momenta of all reconstructed PF objects in an event. Its magnitude is referred to as missing transverse momentum (p_{T}^{miss}). The p_{T}^{miss} performance is shown in Fig. 12 [25]. A resolution of about 25 GeV is achieved in the perpendicular component using PUPPI, with the upgraded detector in events containing a mean PU of 200. For comparison, the corresponding resolution in Run 2 is indicated by the dotted magenta line. There is a modest degradation of the resolution with increasing PU density.

Finally, the identification of jets originating from *b*-quarks, *b*-tagging, is a crucial component of various HL-LHC analyses, including searches for di-Higgs production. The *b*-tagging performance is characterized by rejection (the inverse of the probability to misidentify an object as a *b*-jet) of light-flavor jets and *c*-jets as a function of *b*-tagging efficiency (the probability to correctly identify an object as a *b*-jet).

Heavy-flavor identification in CMS relies on a deep-neural-network algorithm, denoted DeepJet. It is based on kinematic and lifetime information from up to four secondary vertices per jet, as well as on various properties of the charged and neutral particle-flow jet constituents [27]. In very high pile-up conditions, secondary vertex b-tagging is degraded by the formation of spurious secondary vertices caused by pile-up tracks, reducing the ability to distinguish signal from background. The DeepJet algorithm has been retrained in Phase-2 high PU conditions using simulated multijet QCD events and $\mathrm{t\bar{t}}$ events. The b-jet tagging efficiency is shown as a function of the local PU density in Fig. 13 for the fixed misidentification probability. Results with nominal and narrow beam spots (BS) are presented. The efficiency loss due to PU is observed to be only a few percent, both in the barrel and endcap regions of the Phase-2 CMS detector, while the overall efficiency is increased for narrower beam spots.

The ATLAS *b*-tagging algorithm used in the studies is MV2c10 that was developed in Run 2 and adapted for the Inner Tracker (ITk) layout [28, 29]. It relies on a combination of track-based algorithms that make use of large impact parame-

[4] i.e. the vector which when added, balances the transverse momenta of the event.

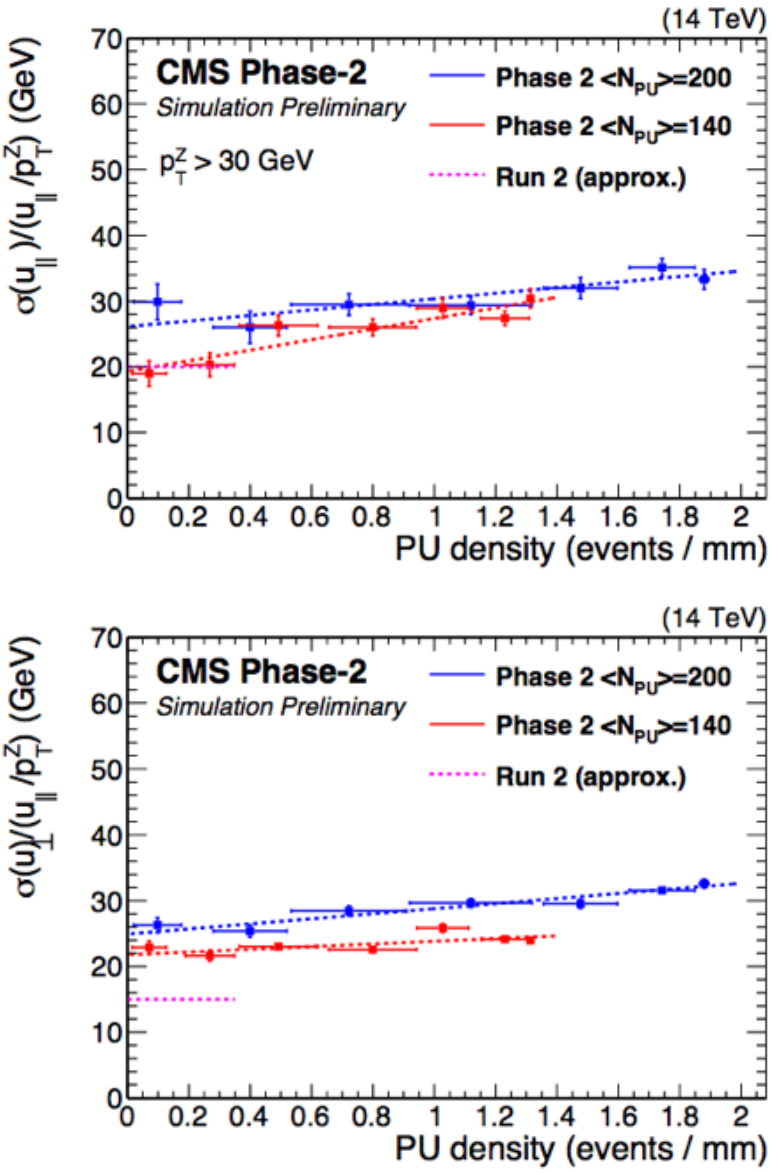

Figure 12: Parallel (top) and perpendicular (bottom) p_{T}^{miss} resolution is shown as a function of PU density in $\mathrm{Z} \rightarrow \mathrm{gg}$ events using the PUPPI mitigation. The blue points indicate the Phase-2 performance with a mean 200 PU, the red points indicate the Phase-2 performance with a mean 140 PU, and the pink dashed line indicates the Run 2 performance with a mean 27 PU. A mild degradation in performance is observed for Phase-2. Taken from Ref. [25].

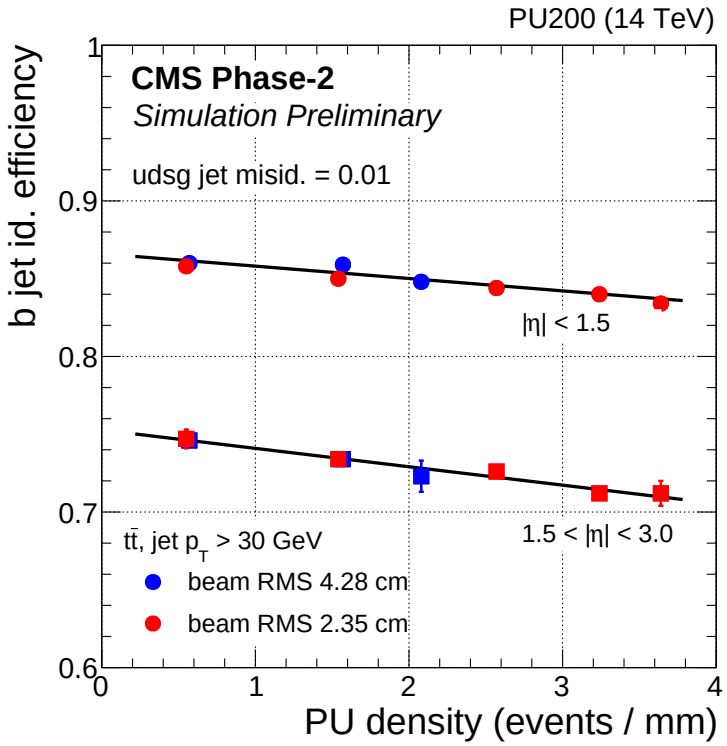

Figure 13: Efficiency of b-jet tagging as a function of the local PU density, using the DeepJet algorithm applied in $t\bar{t}$ events. The misidentification probability for light-flavour jets is fixed at 0.01. Linear fits are superimposed for the barrel and endcap pseudorapidity regions [14].

ter tracks originating from b-decays, and algorithms based on secondary vertices. As both are affected by the presence of additional tracks, pile-up is expected to deteriorate the algorithm performance, especially in the forward region where the impact-parameter resolution is worse. Furthermore, since the algorithm efficiently suppresses the tracks originating far away from the hard-scatter PV, the b-tagging performance is expected to depend mainly on the presence of pile-up vertices near the PV, i.e. be more sensitive to pile-up density than the overall amount of pile-up.

To study the dependence of the performance as a function of the pile-up density, the b-tagging operating point (the selection cut on the algorithm output) was adjusted in pile-up density bins such that corresponding light-jet rejection remained the same for all bins. The resulting b-tagging efficiency is shown in Figure 14 as a function of pile-up density. The b-tagging efficiency at fixed light-jet rejection decreases by about 1% per unit PU density with some indication of a faster drop at very high PU density, though this has not been conclusively demonstrated.

3.4 Impact on physics performance

ATLAS and CMS have an extensive physics program for HL-LHC in which they intend to make measurements of the production and decay modes, and properties of the Higgs boson with high precision, access its rare decays, and carry out a broad program of other SM measurements and searches for beyond-SM physics. The Higgs boson pair (HH) production is one of the most interesting physics processes that can be studied at the HL-LHC, since it is directly sensitive to the Higgs self-coupling. Because of its small production cross section in the standard model (SM) it has not yet been observed at the LHC. Even at the HL-LHC, it may require the combination of various decay channels to reach a level where observation can be declared.

Given its large branching ratio, $HH \to b\bar{b}b\bar{b}$ is a crucial channel for the di-Higgs measurement, despite the experimental challenges associated with it. The impact of the HL-LHC running conditions on the sensitivity of this channel has been studied in ATLAS by extrapolating from the ATLAS Run-2 results with 24.3 fb^{-1} of 13 TeV data. Four b-tagged, central jets with $p_{\mathrm{T}} > 40$ GeV are paired to construct two Higgs boson candidates. The acceptance times efficiency of the full event selection for the SM signal is of 1.6%, and around 95% of the background consists of multi-jet events, which is modeled with data-driven techniques, while the remaining 5% of the background originates from $t\bar{t}$ processes.

As shown in the previous section, the higher pile-up density results in degraded flavor-tagging performance: at fixed mistag rate, the b-tagging efficiency decreases by a relative factor of 2.4% when the peak PU density is increased from 1.7 events/mm to 3.3 events/mm. To evaluate the effect of this degradation on the

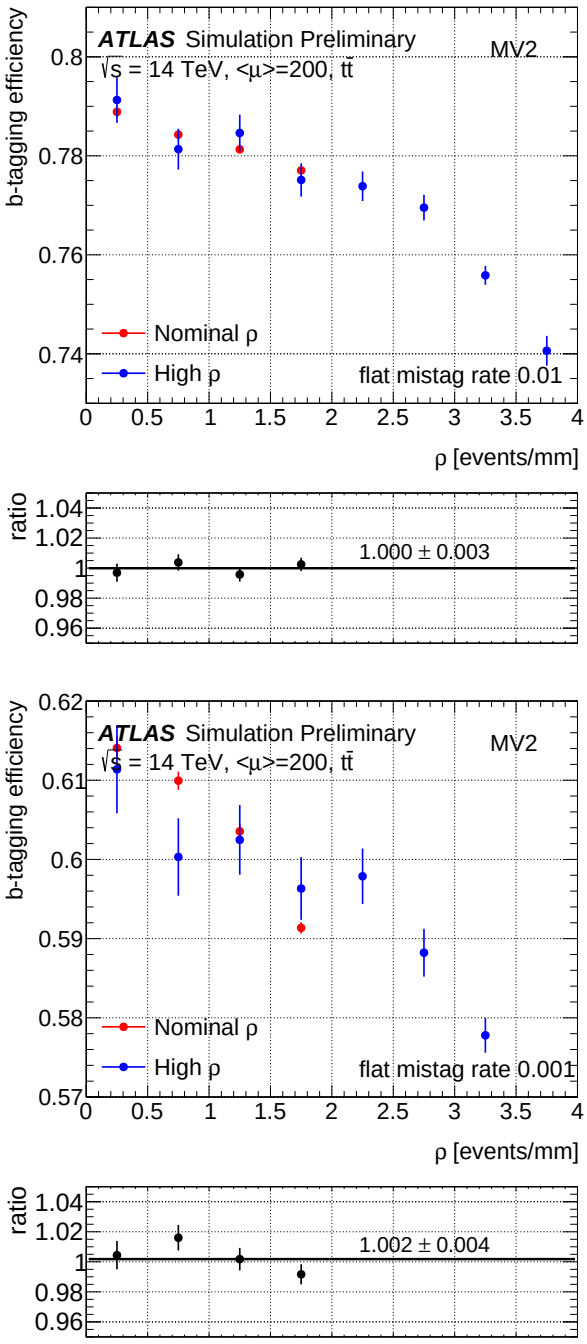

Figure 14: Efficiency for correctly tagging b-jets with $p_{\mathrm{T}} > 20\,\mathrm{GeV}$ and $|\eta| < 4$ in $t\bar{t}$ events as a function of pile-up density at fixed light-jet rejection of 100 (top) and 1000 (bottom) for samples with nominal and high average pile-up density. Taken from Ref. [21].

sensitivity of the $HH \to b\bar{b}b\bar{b}$ measurement at HL-LHC, an event-by-event scale factor for the yields for both the signal and background processes has been computed to account for the lower b-tagging efficiency. The dominant multi-jet background, contributing to $\sim$95% of the total background, has been scaled according to its actual flavor composition derived from simulation. The overall correction factor is 0.9151 for the dominant multi-jet component, and 0.9063 for the signal and the sub-dominant background, primarily composed of $ttbb$ events.

Based on this the expected significance for two values of PU densities were evaluated by generating an Asimov dataset. The degradation in b-tagging efficiency results in a lower significance by $\sim$4%. The loss in significance due to b-tagging in high pile-up density environments can be compensated for by collecting 340 fb^{-1} of additional data. This matches the naive extrapolation from a 10% loss in signal efficiency.

In the CMS case production of Higgs boson pairs decaying to a pair of b-jets and two photons, HH$\to$bb$\gamma\gamma$ is studied. Among various final states explored by CMS as reported in Ref. [30] this decay mode demonstrates the highest sensitivity. The final state contains two b-jets with $p_{\mathrm{T}} > 25$ GeV and two photons with $p_{\mathrm{T}} > 35(25)$ GeV for the leading (subleading) photon, respectively. The threshold for photons are tuned corresponding to the offline requirement of $p_{\mathrm{T\,lead.}} > m_{\gamma\gamma/}/3$, $p_{\mathrm{T\,sublead.}} > m_{\gamma\gamma}/4$. Detailed descriptions of Monte Carlo samples, event selection and the analysis strategy are provided in Ref. [30].

To estimate the effect of PU density on the analysis sensitivity, the efficiencies of reconstructing various objects is fitted with a linear function to provide scaling factors as a function of PU density, as presented in Table 3. The region 1.5-2.0 is considered as "nominal" PU density, whereas 3-4 is the "high" PU density region. This selected analysis only considers photons and b-jets. The expected loss in yield of signal events is summarized in Tab. 4 together with the expected sensitivity of the analysis. Analysis performance in the high PU density regime suffers from an approximate 10% loss of signal events compared to "nominal" PU, with an accompanying degradation in sensitivity.

Object	Difference in efficiency, CMS			
PU density	1.0–1.5	1.5–2.0	2.0–3.0	3.0–4.0
Muons	1.02	1	0.98	0.96
Photons	1.01	1	0.99	0.98
Taus	1.01	1	0.99	0.97
b-jets	1.01	1	0.99	0.97

Table 3: Relative difference in the objects efficiency as a function of PU density relative to the PU density 1.5–2.0 and for fixed misidentification probability

HH $\rightarrow bb\gamma\gamma$ analysis, CMS				
PU density	1.0–1.5	1.5–2.0	2.0–3.0	3.0–4.0
Difference in yield	1.04	1	0.96	0.9
Physics sensitivity, σ	1.85	1.83	1.80	1.75

Table 4: Relative difference in the analyses signal yields as a function of PU density relative to the PU density 1.5–2.0 and for fixed misidentification probability and correspondent sensitivity of analyses.

3.5 LHCb performance and IP parameters

LHCb is an experiment aiming to search for new physics in the precision measurement of b-hadron decay and CP-asymmetries. The second upgrade of the LHCb experiment is envisaged to take place in LS4, with the aim of collecting 300 fb^{-1} by the end of Run 6 [31]. Preliminary studies showed that the LHC can in principle deliver the requested LHCb upgrade instantaneous luminosity of 1.5×10^{34} cm^{-2}s^{-1} [32]. Detailed studies on the beam and operation conditions, along with studies on possible implementation of the required layout and hardware modifications would need to be performed to fully validate and integrate the LHCb upgrade to the HL-LHC baseline.

At a given fixed instantaneous luminosity, the LHCb detector performance will depend on the beam interaction point (IP) characteristics such as the beam crossing angle and the RMS beam size at the IP. The dependence of the LHCb performance on beam parameters has been reported in Ref. [33], and the results are summarized here.

- **Primary Vertex Association:** The performance of the detector depends on the ability to associate reconstructed long lived particles trajectories with the Primary Vertex (PV). If a wrong primary vertex is associated with the b-hadron, the decay time will also be wrong. As shown in Fig. 15 and Fig. 16, at a fixed luminosity of 1.0×10^{34} cm^{-2}s^{-1} the PV misassociation fraction depends on the beam crossing angles and RMS size. The effect can be partly mitigated by adding timing information from the Vertex Locator (VELO) detector. The best detector performance (PV misassociation) for a given luminosity are achieved when the RMS in space and time of the IP region are maximized.
- **Acceptance false asymmetries:** An important feature of the LHCb detector spectrometer is the vertical magnetic field, and the ability to take data samples with opposite polarities. Indeed a magnet polarity averaged data sample allows many possible detector acceptance asymmetries to be cancelled. However if the initial particle distribution is not left-right symmetric, the ac-

ceptance asymmetries will not cancel in the magnet averaged data sample [34]. A left right symmetric distribution of the incoming particles can be achieved only by beams colliding in the vertical plane. It is important to stress that the total crossing angle at IP8 is the sum of the external crossing angle set at injection and the internal one coming from the kick to the beam by the LHCb dipole spectrometer magnet. To achieve a left-right symmetric initial situation, the best solution would be to have a net crossing angle in the vertical plane. This is illustrated in Fig. 17 where beam induced asymmetries are shown for purely vertical and horizontal crossing angles. The asymmetry observed at large pseudo-rapidity for horizontal crossing angles originates from the limited acceptance in the beam pipe region. In order to best control the systematic errors, it is important to take data in the same conditions for both magnet polarities, to accumulate similar statistics for each, and to have a left-right symmetric IP region.

However the present baseline assumes a net crossing angle with an horizontal component that depends on the spectrometer polarity. A full compensation of the horizontal spectrometer effect would have a substantial cost in achievable luminosity and therefore not further considered [35].

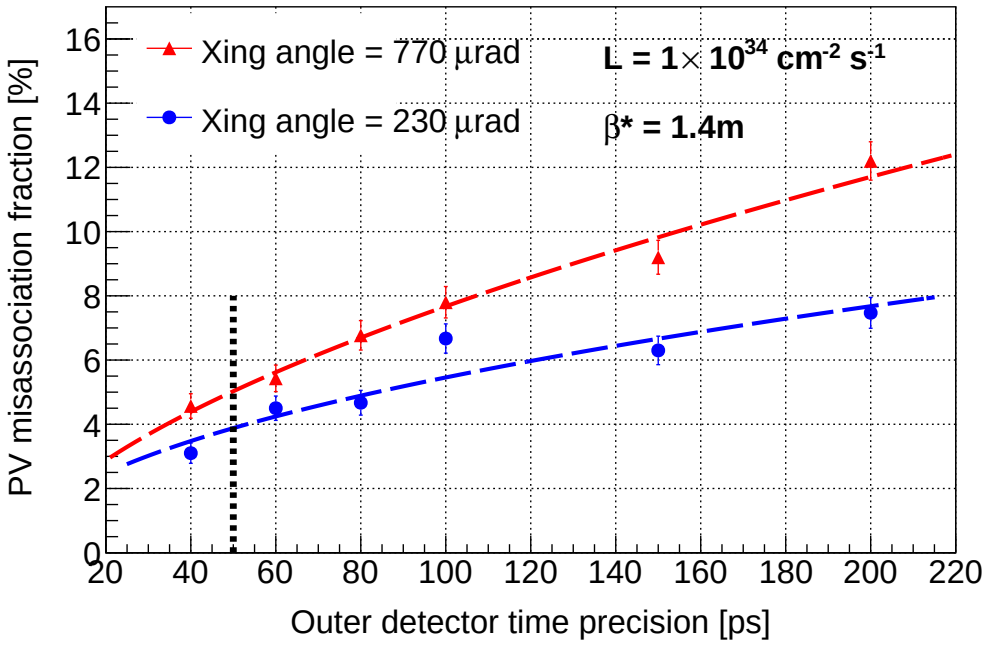

Figure 15: PV misassociation fraction for $B^0 \to \pi^+\pi^-$ decays under different crossing angle values [33]. The results are plotted as a function of the time precision on hits in the outer ($20 < r < 35$ mm) vertex locator, where realistic scenarios are to the right of the vertical dashed line. For this plot, no time information is assumed for the inner ($5 < r < 20$ mm) detector. The (x, y, z, t) RMS values for the pile-up region are: (15.3 μm, 15.3 μm, 51.9 mm, 190 ps) for a crossing angle of 230 μrad, and (15.3 μm, 15.3μm, 32.7 mm, 202 ps) for 770 μrad.

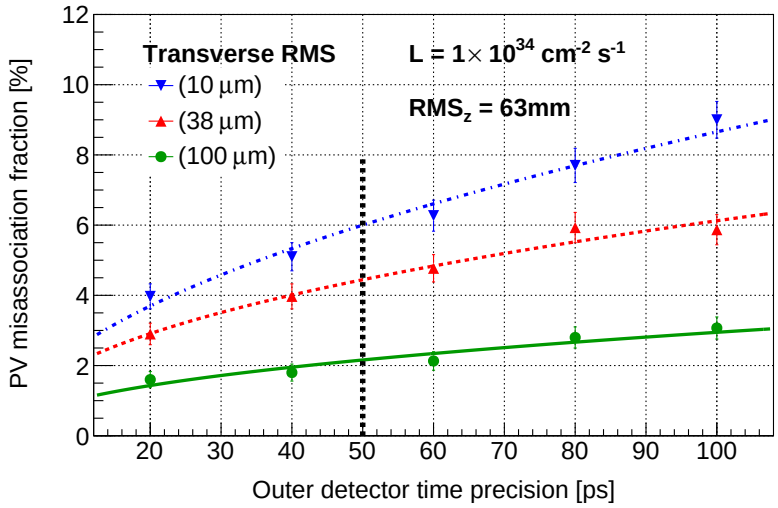

Figure 16: PV misassociation fraction for $B^0 \to \pi^+\pi^-$ decays under different values for the transverse RMS of the luminous region (with longitudinal RMS fixed at $\sigma_z = 63$ mm) [33]. The results are plotted as a function of the time precision on hits in the vertex locator, where the most realistic scenarios are to the right of the vertical dashed line. For this plot, no time information is assumed for the inner detector.

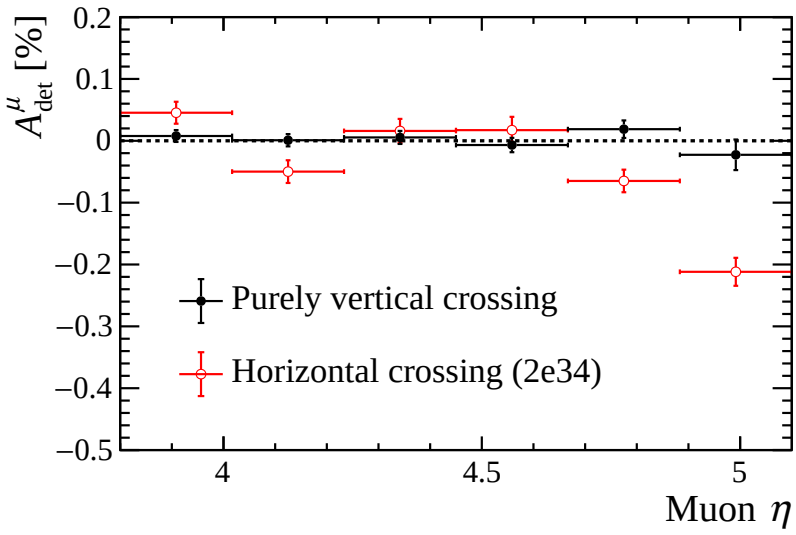

Figure 17: Expected magnet-averaged detection asymmetry due to the geometrical acceptance only, for two different beam-crossing scenarios [33].

4 Bunch-to-bunch Luminosity Fluctuations

For the HL-LHC operation, the luminosity delivered to the high-intensity experiments is leveled for an initial time period, required both to limit the energy deposition by collision debris in the interaction region magnets and to limit the instantaneous peak pile-up in the detectors [4]. This luminosity leveling, achieved in the baseline scenario by dynamically varying the β^* in time, is driven by the average luminosity from all bunches such to maximize the data throughput in the experiments. Variations in the bunch-to-bunch luminosity while levelling may impact the detector performance. For example, bunches with higher luminosity and therefore higher pile-up, may introduce dead-time or loss of data by the data-acquisition system due to the non-linearity in the experiment trigger menus. Ideally the beam-induced fluctuations in the bunch luminosity should remain comparable to the natural variations from the collision statistics, corresponding to $1/\sqrt{n}$ or 8.4(7.0)% for the nominal(ultimate) operation with 140(200) pile-up events.

Variations in the bunch-to-bunch luminosity result mainly from variations in the bunch intensity and transverse emittance. The instantaneous bunch luminosity is defined as:

$$\mathcal{L}_{b,inst} = \frac{f N_1 N_2}{2\pi \sqrt{\beta_x^* \beta_y^*} \sqrt{\varepsilon_{1x} + \varepsilon_{2x}} \sqrt{\varepsilon_{1y} + \varepsilon_{2y}}} \, S, \tag{3}$$

with S a factor depending on the bunch length σ_s, the spot size in the crossing plane $\sigma_\times$, and the crossing angle $\phi_\times$, and assuming that the $\beta_{x,y}^*$ values are equal for both beams. Considering equivalence between the two beams and no correlations, differentiating Eq. (3) we obtain for the bunch-to-bunch luminosity variations:

$$\frac{\delta\mathcal{L}}{\mathcal{L}} = \sqrt{2\left(\frac{\delta N}{N}\right)^2 + \frac{1}{8}\left(\frac{\delta\varepsilon_x}{\varepsilon_x}\right)^2 + \frac{1}{8}\left(\frac{\delta\varepsilon_y}{\varepsilon_y}\right)^2}, \tag{4}$$

Figure 18 shows graphically the dependence of the bunch-to-bunch luminosity variations on the bunch intensity and transverse emittance according to Eq. (4). In Run 2, an excellent performance in the beam preparation was demonstrated, as shown in Fig. 19 [36]. Averaging over several fills, the variation in injected bunch intensity was approx. 4.0%, while the variation in the transverse emittance was around 5%.

Effects at injection energy and during the acceleration ramp result in a sizeable blow-up in the transverse beam emittance and additional bunch-to-bunch fluctuations as summarised in Table 5. The resulting bunch-to-bunch luminosity variation at the start of collisions was around 10%, as shown in Fig. 20.

A key contribution to the bunch-to-bunch fluctuations in LHC is the presence of the electron cloud, or e-cloud. The e-cloud is a beam-induced effect, requiring

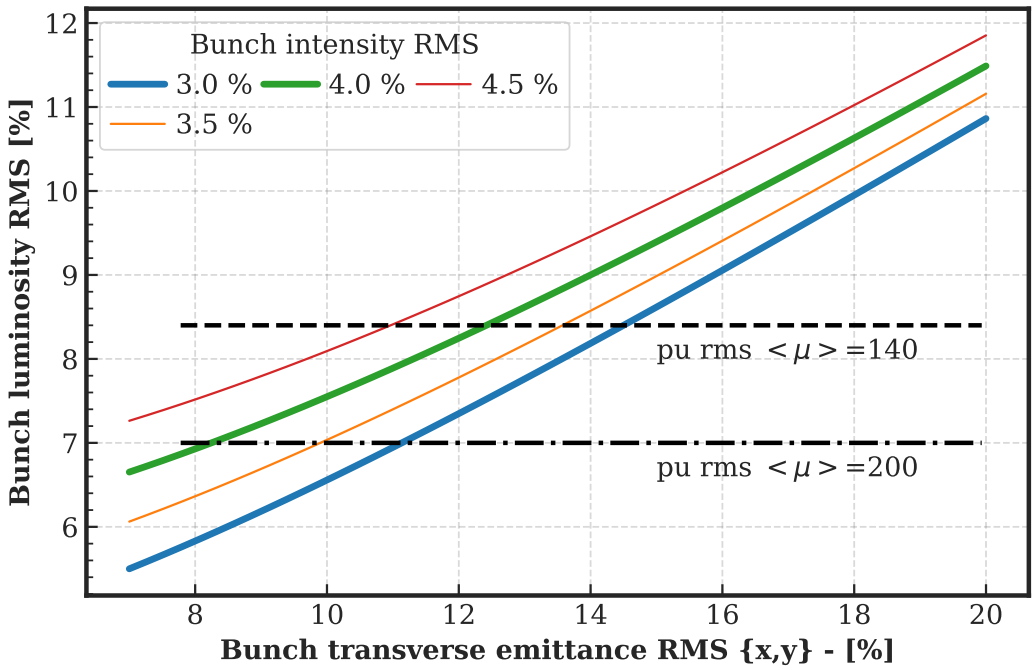

Figure 18: Bunch-to-bunch luminosity variation dependence on bunch emittance and intensity variations. The horizontal lines indicate the 1-sigma variations in the pile-up events during HL-LHC operation. The thick green line indicates the achieved value in Run 2, while the thick blue line the target value for HL-LHC operation.

	beam	**Injection**	**Collisions**
Intensity [%]	B1	4.09	4.46
	B2	4.08	4.26
Emittance [%]	B1-H	4.80	6.59
	B1-V	4.64	7.42
	B2-H	4.97	13.28
	B2-V	5.11	9.52

Table 5: Evolution of the bunch relative intensity and emittance distribution RMS during injection and acceleration, using data from of all physics fills of 2018.

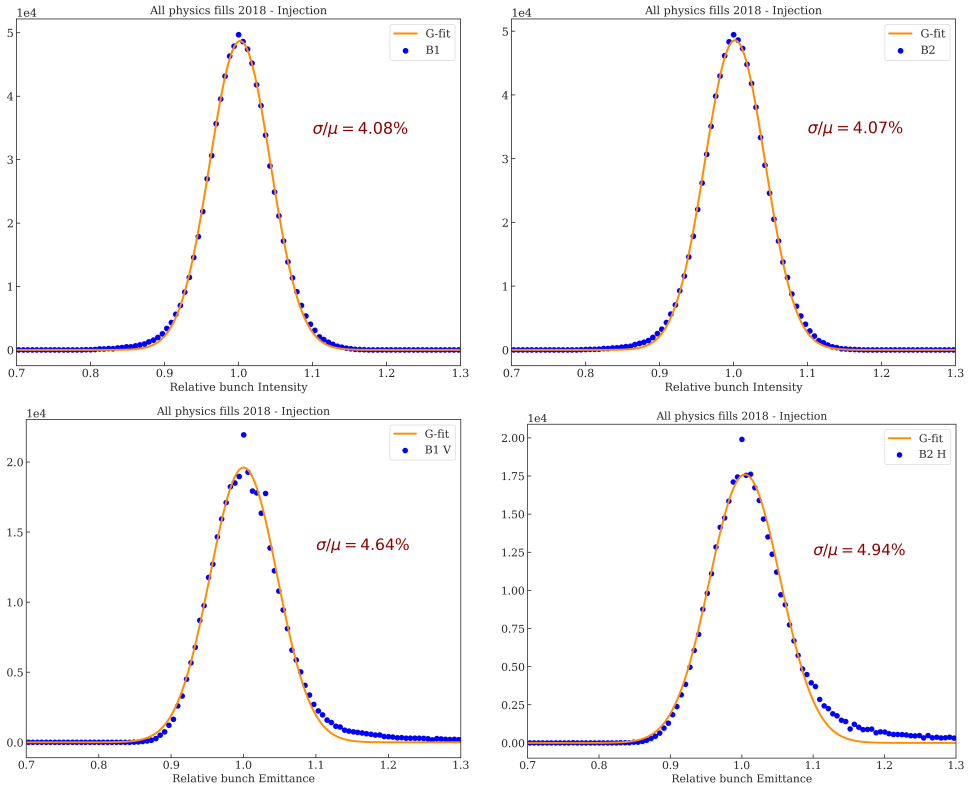

Figure 19: Distribution of the relative bunch intensity (top) and transverse emittance (bottom) at injection from 263 fills with more than 2500 bunches in 2018. The bunch data are normalized to the mean of all bunches per fill.

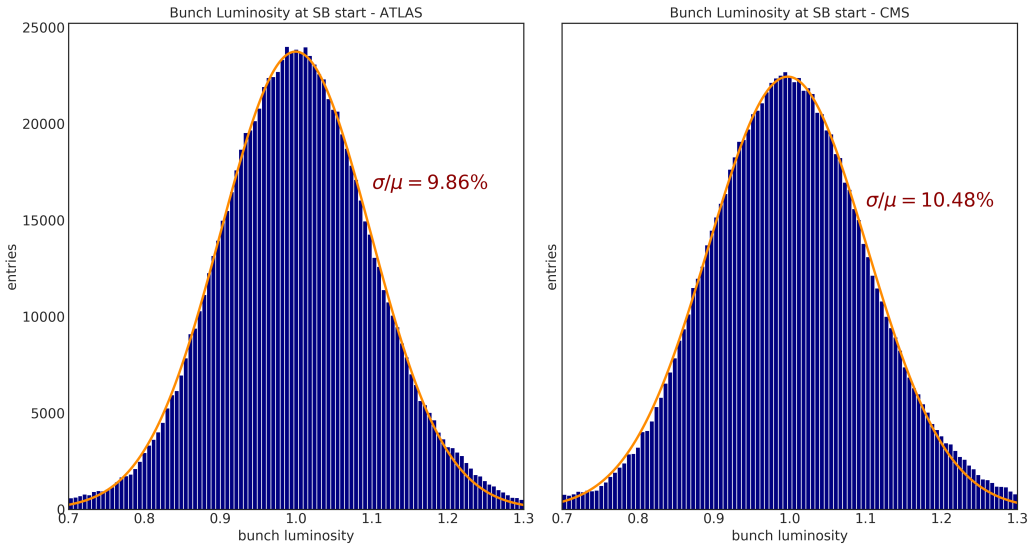

Figure 20: Bunch luminosity distribution at start of collisions for all 2018 fills.

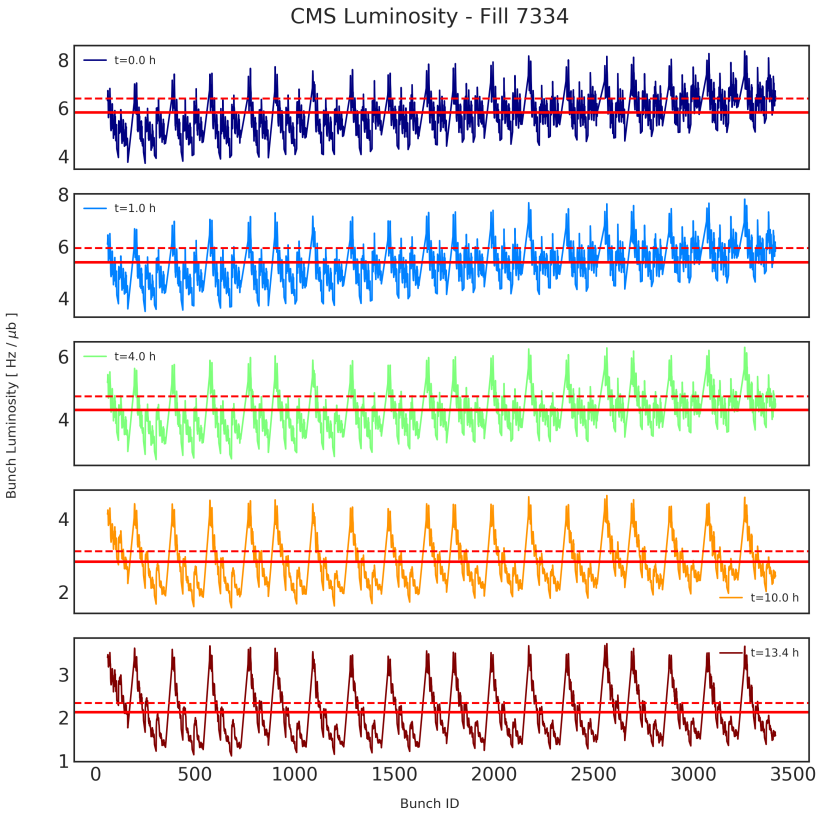

Figure 21: Bunch luminosity variation versus time in collisions for typical physics fills in 2018. The lines indicate the average and $\pm 10\%$ values from all bunches.

the presence of some high-intensity bunches to build-up and then affecting the following bunches. As the beams in LHC are structured in bunch trains of variable length and gaps between them, the e-cloud effectively creates bunch-train position dependent intensity losses or emittance blow-up seen as luminosity variations at the experiments. Other effects like long-range beam-beam interactions and asymmetric burn-off [37] also contribute to bunch-dependent luminosity variations in the LHC.

Figure 21 shows the bunch-by-bunch luminosity in CMS for a typical fill for a range of time instances during collisions. Two effects are visible: first, an initial overall slope at t=0 that is correlated to the time the bunches spent at injection energy (low bunch numbers are injected first and consequently end up with lower intensity) which is then flattened with time in collisions; second, a pattern within the bunch trains that is amplified with time in collision. The latter is best seen in Fig. 22 that shows the bunch luminosity distribution versus time in collision where sub-structures are clearly visible. The impact of the various beam dynamic effects

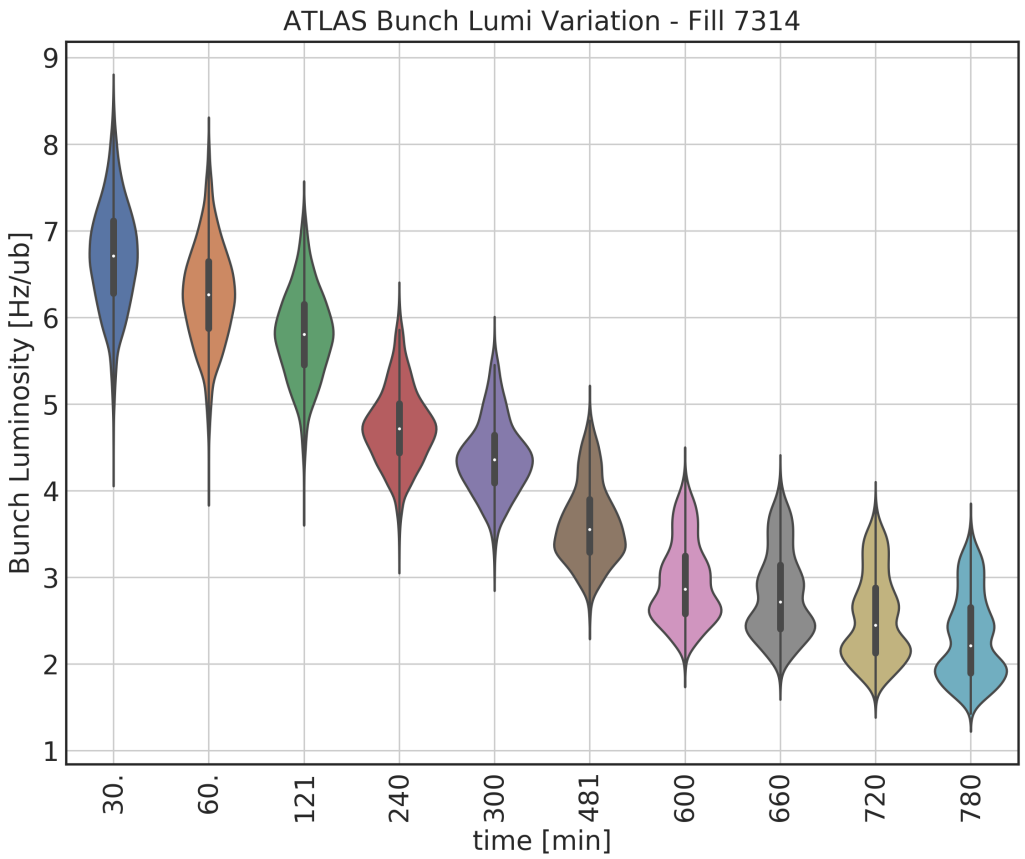

Figure 22: Bunch luminosity distribution versus time in collisions measured in ATLAS for a typical physics fill of 2018.

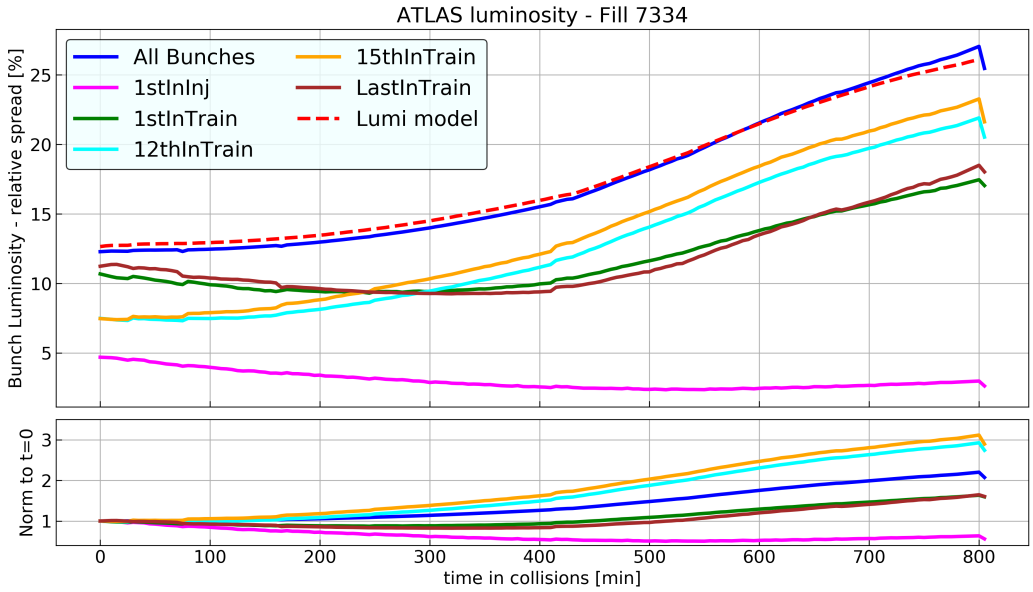

Figure 23: Evolution of bunch luminosity distribution RMS with time in stable beams (SB) collisions, for the five selected bunch families as explained in the text.

that contribute to the development of bunch-to-bunch variations is evaluated by separating the bunches in families according to their position in the trains:

i the 1st bunch of the 1st train in each injection from SPS, which since it comes after a long gap has minimal number of long-range eam-beam (LRBB) interactions and is not affected by e-cloud,

ii the 1st bunch in each of the following trains in the injection, which comes after a small gap, thus has a higher number of LRBB interactions, and some impact from e-cloud,

iii the 12th bunch in the trains that has the average LRBB interactions and is affected by higher e-cloud,

iv the 15th bunch in the trains that has maximum LRBB interactions and e-cloud, and

v the last bunch in each train which has the same low number of LRBB as in family ii) but is fully affected by e-cloud.

Their distinct behaviour is clearly demonstrated in Fig. 23. Comparing the evolution of families ii) and v) with that from families iii) and iv) we can conclude that it is the combined effect of e-cloud and beam-beam that causes the larger intensity losses and thus variations in the bunch luminosity.

Considering all bunches, the RMS luminosity spread shows an increase from 12% to approx. 25% after ten hours in collisions. In Run 2 no luminosity levelling was applied and the luminosity was decaying with the burn-off. Thus the experiments had lots of margin to absorb the increase in variation of the bunch luminosity. In HL-LHC this situation will not be the same, as the luminosity will be levelled optimally to the maximum affordable data rate value. Thus the build-up of bunch-to-bunch luminosity variations with time need to be carefully considered. However, for HL-LHC operation, mitigation measures for the e-cloud are planned such as adding a low secondary electron yield coating to the vacuum chambers in the inner triplets, which from studies so far should eliminate a large fraction of the effect. [38]

4.1 Luminosity fluctuations impact on experiments

The luminosity leveling process will maintain the desired average pile-up. However, any increase in bunch-by-bunch variations will have a detrimental effect on the experiments as not everything degrades linearly with pile-up. The trigger systems, in particular the hardware trigger levels, will tend to preferentially select events with higher pile-up and multi-object triggers and whole event triggers, such as missing transverse energy triggers, tend to be highly non-linear. Increasing bunch-by-bunch variations will therefore both increase the trigger rate (for a fixed set of trigger selections) and the average pile-up in the triggered events. The latter will increase the event size, which largely scales linearly with the pile-up, with the associated readout bandwidth increasing even faster. With sufficiently large variations, either the trigger rate or readout bandwidth limit for some component will be reached, and trigger selections will have to be tightened to avoid dead-time, at the cost of efficiency for the affected physics channels.

The trigger selections for HL-LHC are not yet fully defined and their dependence on pile-up is not known yet. In some cases the use of tracking in the first level trigger will help reduce the pile-up dependence as objects can be required to point to the same vertex. To study the potential impact a toy study was performed with two different assumptions on the pile-up dependence of the trigger, see Table 6. Different bunch by bunch variations are simulated by varying the RMS μ from 0 to 20% and by making up to 20% of the bunches have up to 75% higher μ than the rest, while keeping $\langle\mu\rangle$=200 when averaged over all bunches. For each bunch configuration, the increase in trigger rate is calculated with respect to a flat $\mu = 200$ configuration. This is shown as a function of the RMS of the actual number of collisions per event for the configuration in Fig. 24. In the top half of Fig. 24, the trigger rate is largely independent of the details of the bunch configuration and depends mostly on the RMS. Note that the minimum RMS is 7% due to the intrinsic Poisson fluctuations coming from the collision probability

Dependence	Trigger cfg. 1	Trigger cfg. 2
Linear	25%	40%
Second order	50%	30%
Fourth order	25%	20%
Exponential	0%	10%

Table 6: Two toy trigger configurations are defined where the trigger acceptance has four different components. These components each has a different dependence on the number of pile-up collisions in an event. Fractions are specified as the total component of triggered events for events with 200 overlapping collisions.

at $\mu = 200$. Assuming the data size and the therefore required readout bandwidth scales linearly with the number of collisions in an event, i.e. ignoring the intrinsic overhead in the data format headers etc., one can also calculate the increase in the required bandwidth as shown in the bottom half of Fig. 24.

CONSTRAINTS TO INJECTED BUNCH PARAMETERS

The trigger and readout system of the experiments will have some operational margin to handle variations from run to run or during a run, but should be kept at a minimum to maximize the physics output. Allowing a 10% maximum increase in the needed bandwidth would require the pile-up RMS to remain below **12%, (possibly up to 15%)** according to the trigger configuration examples of Figure 24. Accounting for the intrinsic Poisson fluctuations, this means that the bunch-by-bunch luminosity variations (RMS) should be kept below **9% for the nominal** and **10% for the ultimate** operation parameters of HL-LHC during the period where the luminosity is leveled.

In Run 2 for the corresponding leveling time in HL-LHC of approximately 4 and 1 hour for the two scenarios, there was a growth in the bunch luminosity RMS of 2% and 1% respectively, see Fig. 23. Assuming the same growth in HL-LHC, a pessimistic approach that does not take into account the foreseen mitigation measures, the above requirement translates to an RMS variation of 7% and 8% in the bunch-to-bunch luminosity at the start of collisions, for the nominal and ultimate HL-LHC scenario. Using Eq.4 and Fig. 18 and the data of Table 20, this can be converted into a requirement for the bunch intensity and emittance variations. Setting as goal a **3% variation (RMS) in the bunch intensity at injection**, which is slightly better than the 4% achieved in Run 2 but feasible, the **bunch-to-bunch variation (RMS) in the transverse emittance at start of collisions should be less than 11%, or less than 6% at injection, considering that the foreseen mitigation measures will eliminate a large fraction of the observed variation coming from the emittance blow-up at injection.**

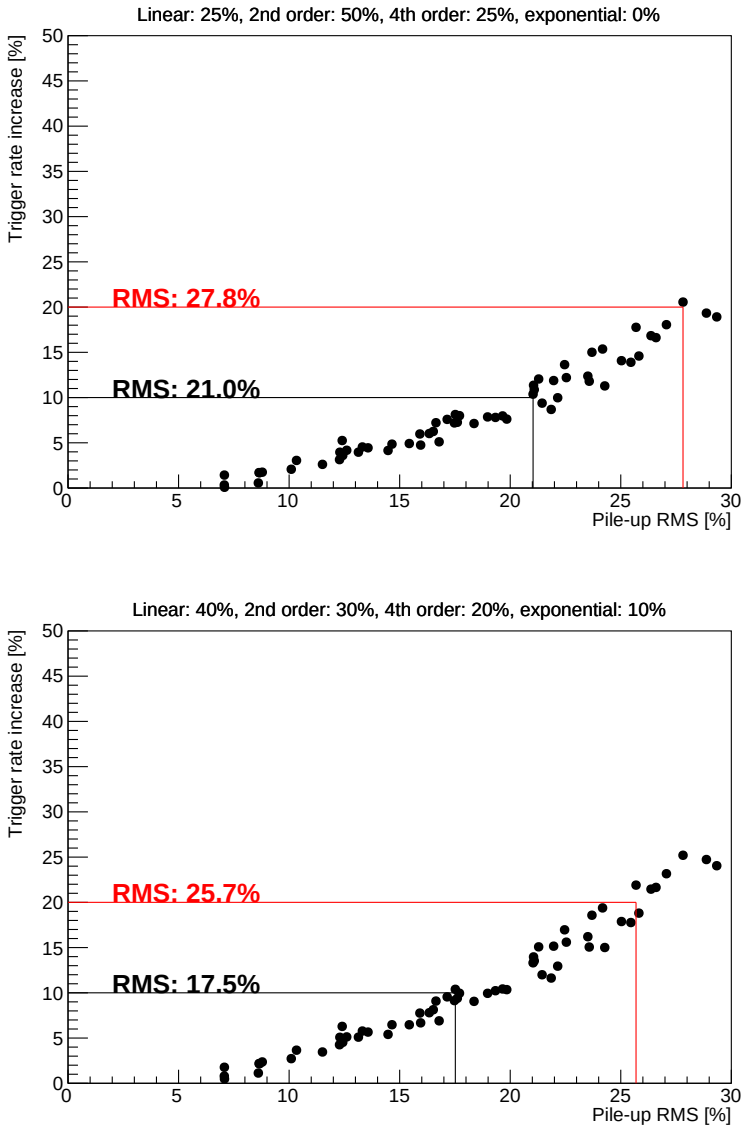

Figure 24: Increase in trigger rates for two different trigger pile-up dependencies (left and right) for different bunch-by-bunch variations, see text. The bunch-by-bunch variations are presented in the form of the RMS of the luminosity variations.

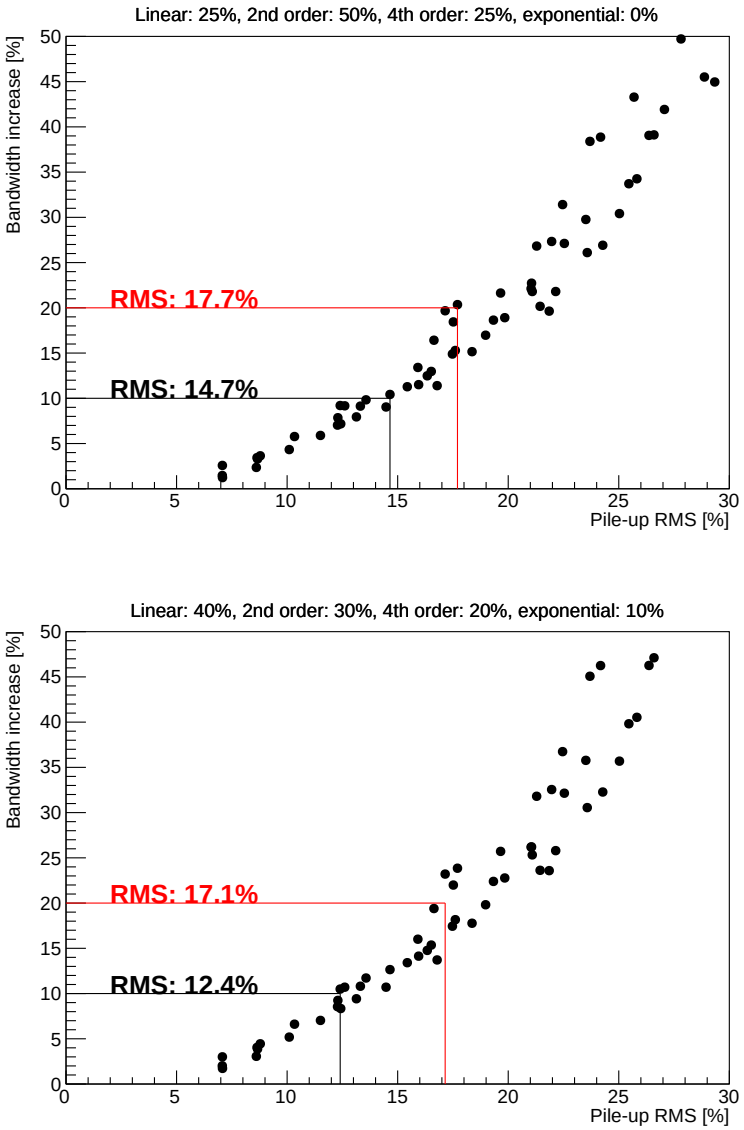

Figure 24: Increase in readout bandwidth for two different trigger pile-up dependencies (left and right) for different bunch-by-bunch variations, see text. The bunch-by-bunch variations are presented in the form of the RMS of the luminosity variations.

Once the luminosity drops below the peak levelled luminosity, additional bandwidth will naturally become available in the system.

Finally, to complete the discussion, the impact of pile-up density on the ATLAS trigger rates is only expected to be visible in the HLT, as no tracking information is used at the hardware trigger level. The impact in the HLT is expected to be at the same level as for offline analysis.

5 Non-colliding Bunches

In Run 2 the filling scheme during physics collisions included an intermediate-length train that were not colliding in the high-luminosity experiments at IP1 and IP5. The presence of this intermediate length train of non-colliding bunches is important to both the experiments and the accelerator, as explained below, and will remain during HL-LHC operation, in particular during the intensity ramp up.

For the accelerator the intermediate-length bunch train, consisting of 6 to 12 bunches, was introduced in the LHC filling schemes during Run 1 to avoid a large intensity and stored energy steps from one circulating probe bunch to trains of 288 bunches with nominal intensity ($> 10^{11}$ protons). The stored energy of such an intermediate-length train at 450 GeV corresponded roughly to the threshold (10^{12} protons) where damage by beam on a Copper vacuum chamber becomes possible in case of uncontrolled beam loss. The intermediate-length train is specially prepared in the injectors that besides its length has the same bunch parameters (intensity, transverse and longitudinal emittances) similar to the nominal trains [5], and was typically placed right after the abort gap in the LHC ring.

Since Run 1 the typical LHC filling sequence consists of the following three steps:

- Injection of a probe bunch to setup the machine at injection (tunes, chromaticities and orbits). If necessary, the probe bunches are dumped and reinjected multiple times.
- With one probe bunch circulating in the ring, at least one intermediate-length bunch train is injected. If trajectory excursions and beam losses are adequate, the LHC shift crew proceeds to the next step, else it may decide to perform beam steering and tuning in the injectors (for example transverse scrapping in the SPS) by injecting a sequence of intermediate-length trains. At the end of the tuning the intermediate-length trains are dumped, and the filling sequence is restarted from a probe bunch.

[5] single injection from PSB to PS, following the usual scheme of triple splitting at low-energy and twice double splitting at top energy

- Filling the long trains that are injected one after the other. The probe bunch is eliminated during the filling process either by cleaning out using the injection cleaning function of the transverse damper or by over-injecting during one of the train injections.

The LHC Software Interlock System enforces the injection of the intermediate-length train by comparing the circulating beam intensity in each LHC ring with the beam intensity in the SPS just before the start of the SPS energy ramp. It will block injection of nominal trains if the circulating beam intensity in the LHC is too low (absence of intermediate-length train).

To be able to use the intermediate-length train for beam steering and setup as described above, the bunch characteristics (intensity, emittance and tails) must be as similar as possible to the nominal beam injections. In that case losses may for example be scaled from the intermediate-length train to nominal train length to evaluate if the latter may be injected without risk of beam dump on beam losses. Beam dumps on beam losses above threshold are the main reason for aborts of the injection sequence.

For Run 3 two improvements are foreseen for injection steering and beam losses.

- Some of the highest beam loss signals are generated by showers due to scrapping on transfer line collimators. Those showers hit the LHC ring BLMs from the outside and represent an external cross-talk signal (fake loss) that occurs on a single pass during the transfer. The BLM system firmware has been upgraded during LS2 with a "signal blinding" option around the time of injection. When it is activated the loss occurring in the turns around injection are ignored. This feature may be activated for selected BLMs to render the LHC injection process less sensitive to single pass tail scrapping.
- For safety reasons steering of the transfer lines was so far only performed on intermediate trains (enforced by procedure). In Run 3 it is planned to allow gentle steering also with the nominal injections.

If applied successfully those two changes could help loosening the requirements on intensity and tails between intermediate and nominal trains.

Following requests by the experiments this intermediate-length train bunches were configured not to collide at the high-intensity IPs 1 and 5. In a later overall optimisation of the machine luminosity delivered to the experiments in Run 2, the intermediate-length train bunches had collisions at IP2 or IP8.

For the ATLAS and CMS experiments, the train of the non-colliding bunches provide a measure of the beam induced background (primarily by beam-gas interactions, but also from beam halo cleaning in the TCTs with the produced secondaries reaching the experiments), as well as background from afterglow due to

activation and decay in the experimental detectors, mainly in the forward region. The present choice during Run 2 of the non-colliding bunch train with 12 bunches is a good compromise between the statistics required and the luminosity loss.

During HL-LHC operation, the presence of the non-colliding bunch trains would be needed in particular during the intensity ramp up. The different lay-out of the forward interaction region with larger TAS aperture and the beam halo levels expected due to increased intensity, will result in new background rates in the experiments that need to be carefully studied, evaluated and constantly monitored.

As for the accelerator, the experiments require the bunch parameters of the non-colliding bunches to be similar to the nominal ones to allow easy extrapolation of the results. However this is not easily attained as for example the colliding bunches loose intensity with time in collisions due to burn-off (approx 7%/h in nominal HL-LHC operation from Figure 24a) while the non-colliding do not [6].

Figure 25 compares the intensity and emittance evolution with time in collision of the non-colliding and colliding bunches in a typical LHC fill of Run 2. The evolution of the transverse emittance between the colliding and non-colliding bunches is also different: the non-colliding bunches arrive at the top energy with slightly higher transverse emittances have a reduced blow-up in the horizontal plane, and a large damping in the vertical plane as expected due to synchrotron radiation. However what is important is that the parameters remain similar and at some point in time they will coincide with that from the discussions within the Working Group was concluded as sufficient by the experiments for their studies and measurements.

Another important consideration for the non-colliding bunches is stability. The non-colliding bunches miss the head-on collisions at IP1 and IP5 and therefore lie on a different working point with respect to the other bunches, which may result in instabilities and higher losses. This stability issue can be easily mitigated by a larger transverse emittance for the non-colliding bunches that can be achieved by a blow up using the transverse damper just before starting the acceleration ramp. [39]

Last, at HL-LHC operation another possible use of the non-colliding bunch train at top energy is to monitor the efficiency of Hollow Electron Lens (HEL) collimator. This can be done by comparing the loss rates between the colliding and non-colliding bunches, with the condition that their parameters remain similar to avoid large extrapolation errors.

[6] this would be the case up to LHCb phase 2 upgrade, when an intensity reduction in the non-colliding bunch intensity for the bunch pairs that would collide at IP8 of approx. 2%/hour is expected.

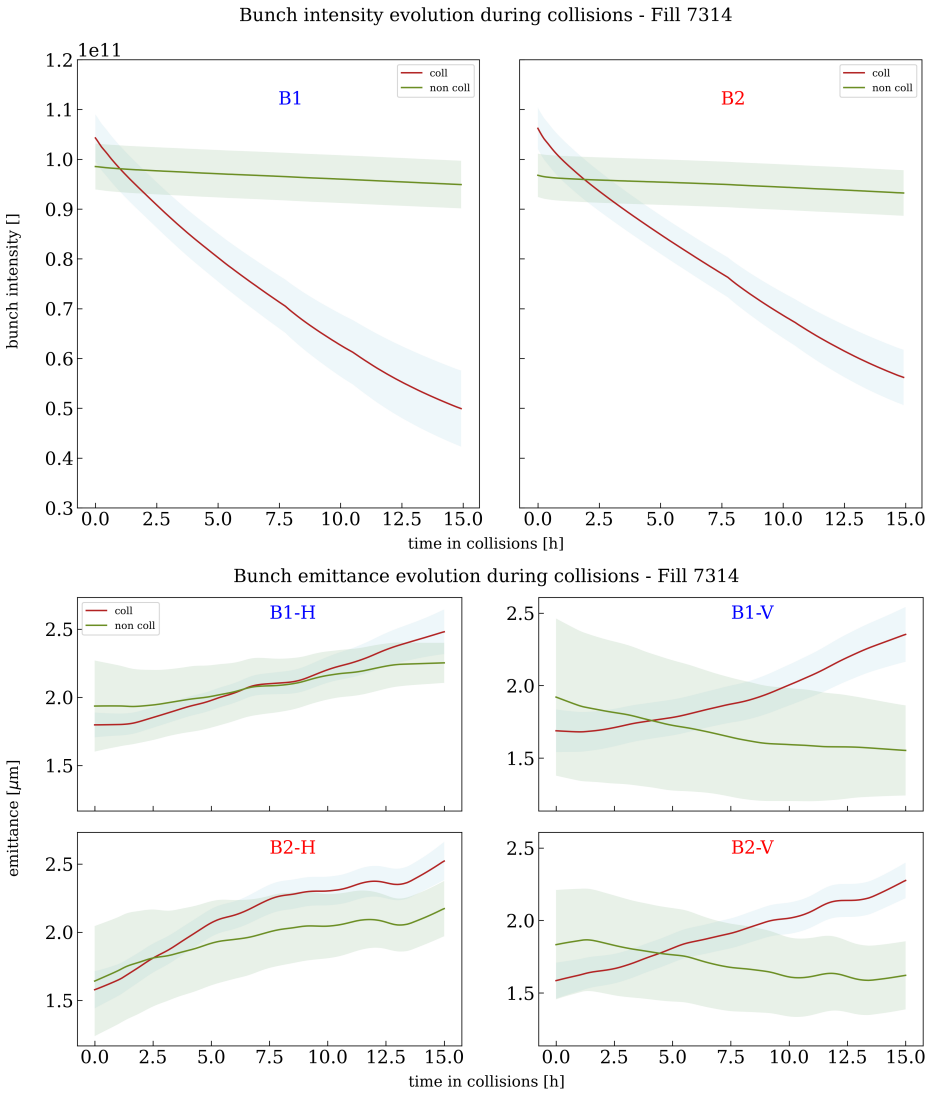

Figure 25: Evolution of bunch intensity (top) and emittance (bottom) for the colliding and non-colliding bunches during collisions in a typical fill of Run 2.

To conclude, the need of the non-colliding bunch train (per beam) is confirmed for HL-LHC operation, first as tuning and intensity bridge at injection energy with nominal bunch parameters and second, after a blow-up of the transverse emittance before the acceleration ramp, for the monitoring of background in ATLAS and CMS experiments and the HEL collimator cleaning efficiency.

6 Luminosity Calibration

The LHC experiments are targeting a systematic uncertainty of 1% on the annual integrated luminosity after final calibration during HL-LHC proton-proton operation. Such a precision will be challenging but will substantially reduce the contribution of the luminosity measurement to the total uncertainty of many key results, in particular for studies of Drell-Yan lepton-pair, top-quark pair and Higgs-boson production. The full physics motivation for this is given in Refs. [40, 41].

The experimental strategy has two pillars: the collection of all the data necessary to determine the integrated luminosity for annual physics data sets with an overall uncertainty of approximately 1%, and a highly stable, online, bunch-by-bunch luminosity measurement with sufficient redundancy to operate in all LHC conditions and capable of an approximately 2% absolute precision in real time. There are two main reasons for the latter. Real-time bunch-by-bunch data give important feedback to the LHC experts to achieve the best machine performance, and to the experiments to tune their trigger settings. The experience of Phase 1 has shown that such online precision helps disentangle instrumental variations of the ATLAS / CMS delivered-luminosity ratio from actual variations in beam parameters, and will be even more important in the presence of luminosity levelling. Moreover, a precise online measurement also allows the continuous validation of the applied methodology and can be used to identify discrepancies between independently calibrated luminometers such that they can be addressed in real time before they become too large, thus preventing data loss and helping achieve the ultimate offline target. Luminosity measurements require two steps: the precise calibration of luminometers under special running conditions, and the propagation of that calibration to physics data-taking conditions, both in terms of the extrapolation to conditions with higher instantaneous luminosity, and of the tracking of time- or exposure-dependent variations in the performance of the luminometers over the extent of the physics data-taking period. Luminosity monitoring and calibration for ion physics is performed using a similar strategy.

The van der Meer (vdM) [42] method, based on beam separation scans in the x and y transverse directions, is used for precise calibration of the luminometers, i.e. for the determination of their visible cross-section in a small number of dedicated LHC fills, typically one or two per running period (i.e. per year and operation

mode). Due to the symmetries of the LHC ring, ATLAS and CMS usually make use of the same fills and perform their various calibrations in an interleaved way. The experiments expect to continue to rely on annual vdM sessions using the same methodologies as in Run-2 [43, 44, 45], but with continuous improvements to be tested and integrated into these programs later in the Run. The LHCb and ALICE experiments have their own set of detectors for online and offline luminosity measurement, and follow similar strategies for their calibration.

Recent studies of the mutual electromagnetic interaction between colliding bunches [46, 47] brought improved corrections to the beam-overlap integral, by accounting more accurately for beam–beam-induced non-linear distortions of the transverse bunch profiles. These calculations shall be experimentally validated as best as possible before the HL-LHC phase.

A leading uncertainty on the visible cross-sections, that is correlated across all luminometers at a given IP and during a given scan, is associated with non-factorization biases.[7] These can be corrected by combining the beam-separation dependence of the luminosity measured in a pair of one-dimensional x-y scans with that of the parameters of the luminous region during the same scans, i.e. with the beam-separation dependence of the position, orientation, size and shape that describe the luminous ellipsoid in three dimensions.[8] A careful preparation of the beams in the CPS, with as a criterion a transverse bunch profile as close as possible to a perfect Gaussian, has been demonstrated to reduce the necessary correction significantly.

LHC beam instruments that measure beam parameters (intensity, transverse and longitudinal profiles, positions, tunes) play a crucial role in luminosity calibrations, thus their improved performance is a necessary condition to achieve the precision goals. This is particular true not only of precision bunch-current measurements, that directly influence the absolute luminosity scale, but also of beam-position measurements. The LHC beam-position monitors (BPMs) are used to

[7] The original van der Meer formalism assumes that the particle densities in each bunch can be factorized into independent horizontal and vertical components, such that the overlap integral of the two beams, i.e. the specific luminosity $\mathcal{L}_{sp}$, is given by the inverse product of the horizontal and vertical convolved beam sizes Σ_x, Σ_y that are extracted from, respectively, a horizontal and a vertical vdM scan:

$$\mathcal{L}_{sp} = f_r / 2\pi\Sigma_x\Sigma_y$$

where f_r is the LHC revolution frequency. When this is not the case, i.e. when the transverse density distributions are affected by non-linear x-y correlations, the overlap integral calculated from the above formula, and therefore the absolute luminosity scale, may be biased by up to a few percent.

[8] An alternative proposed by LHCb is to measure the specific luminosity over a two-dimensional grid in the transverse-separation plane: this allows the calculate the overlap integral directly by integration over that plane.

correct luminosity calibrations for orbit drifts on time scales of a few ten seconds to an hour, be it in the context of baseline, factorizable vdM fits to luminosity-scan curves, of non-factorization corrections, or of length-scale calibrations. More recently, BPMs have also proved essential in diagnosing and accounting for the impact of magnetic non-linearities in the steering correctors that make up the closed-orbit bumps used during vdM scans. The requirements set by the experiments on the upgraded BPM system for HL-LHC, in view of their use during vdM scans, have been incorporated into the "Conceptual Specification for the BPMs in the HL–LHC era" [48].

All luminometers suffer from some degree of non-linearity, that must be measured and accounted for when extrapolating the visible cross-section from the vdM environment to physics data-taking. This will mean an extrapolation over a factor of 400 in the single-bunch instantaneous luminosity (SBIL) for HL-LHC parameters. Typical contributions to the non-linearity of luminometer response come from rate-dependent efficiency, timewalk, albedo, and afterglow effects. Each of these can, in turn, also be subject to time-dependent variations from detector or electronic aging, the effects of cumulated radiation dose (which can influence the stability of certain detectors), changes in operating conditions and the choice of the filling scheme.

CMS has demonstrated [49, 45] the benefits of emittance scans [50], which are short vdM-like scans taken at the beginning and the end of all physics data-taking fills to charracterize non-linearity and stability effects. ATLAS has relied less on emittance scans for their Run-2 analysis, but is also interested in exploiting them. While the systematic uncertainties in these scans are not yet measured at the level necessary to extract the absolute visible cross-sections with sufficient precision, they allow the derivation of effective (i.e. relative) visible cross sections for a luminometer throughout the year when data are taken in similar conditions. These bunch-by-bunch measurements can be used to determine the effective visible cross section as a function of SBIL, thereby making it possible to quantify non-linear effects as well as monitor the efficiency over time from the visible cross-sections extrapolated to the intercept (SBIL=0). Efficiency and linearity corrections based on the observed trends are extracted entirely independently for each luminometer. A requirement for emittance scans is that the scans pass through the head-on point in both transverse coordinates. This is not practical when separation levelling is in use, but is not a problem during $\beta^\star$ levelling, as is the expected baseline for HL-LHC operation.

In summary, the experimental strategy [40, 41] for luminosity measurement is to have multiple, independently vdM-calibrated, bunch-by-bunch luminometers at each experiment, continuously monitored by emittance scans. This will allow the non-linearity and the efficiency of each luminometer to be tracked independently. By analysing the data from μ scans (vdM-like scans under physics-like

beam conditions, possibly with a reduced number of colliding bunches), as well as the measured luminosity ratios during physics fills for all pairs of luminometers, the residual systematic uncertainties can be quantified. A combination strategy for all luminosity measurements, which requires accounting for the correlations between all sources of uncertainties across the luminometers, is also under study to optimally use the collected information so as to reach the targeted 1% accuracy on the luminosity. The program relies on continuous, precise, LHC beam instrumentation data, a few vdM and μ scans per year, as well as emittance scans at the beginning and end of some physics fills to sample different beam conditions.

7 Summary

Within the course of the HL-LHC Experimental Data Quality Working Group, the impact on the detector performance for different operational scenarios of HL-LHC affecting the luminous region parameters was studied. The key scenarios of HL-LHC operation considered include: a) the **baseline** parameter operation with levelled luminosity at $5 \times 10^{34}\text{cm}^{-2}\,\text{s}^{-1}$, a pile-up of 132 events and a pile-up density in the range of 1.0-1.5 (2.0-2.7) events/mm with the use of crab-cavities (without in parenthesis), and b) the operation at the **ultimate** machine parameters with levelled luminosity of $7.5 \times 10^{34}\text{cm}^{-2}\,\text{s}^{-1}$, a pile-up of 200 events and a pile-up density in the range 1.5-2.0 (3.5-4.0) events/mm, again with and without the use of the crab-cavities.

The impact on the reconstruction efficiency of physics objects like primary vertices, muon, electron, photon or b-jet tagging, was thoroughly studied with the pile-up and pile-up density varying in the expected range. For the majority of the physics objects, the efficiency is slightly dependent on the pile-up level (see Figures 4 and 6). This is not surprising as the upgraded detectors are specially designed and the reconstruction algorithms are tuned to handle the expected high-pileup levels. The major dependence which represents a key challenge for the experiments at HL-LHC operation, arises from the handling of the pile-up density. A linear degradation of the reconstructed efficiency for the physics objects studied was observed for the relevant pile-up density region without displaying abrupt changes (see Figures 8 to 13).

From the CMS study, as summarized in Table 3, the b-jet reconstruction efficiency considering as reference the performance for the baseline operation with CCs, degrades by 2% without the use of CCs, and by 3% in the ultimate scenario without CCs. Similarly, the muon reconstruction efficiency degrades by 4% in the baseline operation without CCs, and by 4% in the ultimate scenario wihout CCs. Beyond the single physics objects, the impact on different physics channels was studied. In this case, the efficiency of the various objects involved in the

analysis is combined. For example in the $HH \to bb\gamma\gamma$ case objects efficiency degradation would result in an overall loss of 8(10)% of events for the baseline(ultimate) operation without CCs, or effective lost of 240(400) fb^{-1} of the planed 3000(4000) fb^{-1} luminosity. A similar study for the ATLAS experiment concluded that the expected degradation for flavor tagging in the high-pile-up-density scenario (i.e. ultimate operation without CCs) will reduce the sensitivity of the $HH \to 4b$ analysis at a level that would require at least 450 fb^{-1} beyond the planned 4000 fb^{-1} in this mode of operation to compensate.

It should be noted that further improvements in the reconstruction algorithms, optimised to the final operational scenario of HL-LHC with respect to the pile-up density will help to partially mitigate the performance loss indicated here.

To ensure a tolerable level of the bunch-by-bunch luminosity variation ($< 9\%$ for nominal HL-LHC parameters) the maximum intensity variation during collision should remain at around 3% while the transverse emittance variation should be below 11%. This translates into a requirement at injection for a maximum of 3% rms variation in the bunch intensity and 6% rms variation in the transverse emittance.

To guarantee beam stability the non-colliding bunches must feature a factor 2 larger transverse emittance with half the intensity of the nominal bunches at the start of the physics fill.

The luminosity calibration will require VdM and μ scans each year, as well as emittance scans featuring large beam-beam offsets at the beginning and end of each physics fill. The emittance scan request could be in conflict with offset luminosity levelling but this is not currently foreseen in the HL-LHC baseline.

Acknowledgments

We thank all the members of the working group and colleagues who participated in the meetings and discussions and have directly contributed to this document with studies and plots. In particular we acknowledge the co-authors and those involved in the production of the document ATL-PHYS-PUB-2021-023 from the ATLAS Collaboration, and CMS-DP-21/026 and CMS-Note-2018/006 from the CMS Collaboration.

We are thankful to Gianluigi Arduini, Oliver Brüning, Rhodri Jones, Yannis Papaphilippou and Markus Zerlauth for the comments, suggestions and proof-reading of the manuscript.

References

[1] R. Tomás, O. Dominguez, and S. White. Hl-lhc alternatives. *CERN in the Proceedings of RLIUP*, CERN–2014–006, 2014.

[2] G. Arduini *et al.* Hl-lhc run 4 proton operational scenario. CERN–ACC-2022–0001, 2022.

[3] Expected pile-up values at HL–LHC. Technical report, 2013.

[4] G. Apollinari, I. Béjar Alonso, O. Brüning, P. Fessia, M. Lamont, L. Rossi, and L. Tavian. *High-Luminosity Large Hadron Collider (HL-LHC): Technical Design Report V. 0.1*. CERN Yellow Reports: Monographs. CERN, Geneva, 2017.

[5] L. Medina, R. Tomás, G. Arduini, and M. Napsuciale. Assessment of the performance of high luminosity lhc operational scenarios: Integrated luminosity and effective pile-up density. *Canadian J. Phys.*, 97:498, 2018.

[6] R. Tomás, J. Keintzel, and S. Papadopoulou. Emittance growth from luminosity burn-off in future hadron colliders. *Phys. Rev. Accel. Beams*, 23:031002, 2020.

[7] D. Contardo, M. Klute, J. Mans, L. Silvestris, and J. Butler. Technical Proposal for the Phase-II Upgrade of the CMS Detector. CMS Technical Design Report CERN-LHCC-2015-010, LHCC-P-008, CMS-TDR-15-02, 2015.

[8] CMS Collaboration. The Phase-2 Upgrade of the CMS Tracker. CMS Technical Design Report CERN-LHCC-2017-009, CMS-TDR-014, 2017.

[9] CMS Collaboration. The Phase-2 Upgrade of the CMS Barrel Calorimeters Technical Design Report. CMS Technical Design Report CERN-LHCC-2017-011, CMS-TDR-015, 2017.

[10] CMS Collaboration. The Phase-2 Upgrade of the CMS Endcap Calorimeter. CMS Technical Design Report CERN-LHCC-2017-023, CMS-TDR-019, 2017.

[11] CMS Collaboration. The Phase-2 Upgrade of the CMS Muon Detectors. CMS Technical Design Report CERN-LHCC-2017-012, CMS-TDR-016, 2017.

[12] CMS Collaboration. The Phase-2 Upgrade of the CMS Level-1 Trigger. CMS Technical Design Report CERN-LHCC-2020-004, CMS-TDR-021, 2020.

[13] CMS Collaboration. Expected performance of the physics objects with the upgraded CMS detector at the HL-LHC. CERN Note CERN-CMS-NOTE-2018-006, 2018.

[14] CMS Collaboration. Experiments Data Quality (CMS). CMS Performance Summary CMS-DP-21/026, 2021.

[15] ATLAS Collaboration. Technical Design Report for the ATLAS Inner Tracker Strip Detector. (CERN-LHCC-2017-005. ATLAS-TDR-025), Apr 2017.

[16] ATLAS Collaboration. Technical Design Report for the ATLAS Inner Tracker Pixel Detector. Technical Report CERN-LHCC-2017-021. ATLAS-TDR-030, CERN, Geneva, Sep 2017.

[17] ATLAS Collaboration. Technical Design Report for the Phase-II Upgrade of the ATLAS Muon Spectrometer. (CERN-LHCC-2017-017. ATLAS-TDR-026), Sep 2017.

[18] ATLAS Collaboration. Technical Design Report for the Phase-II Upgrade of the ATLAS LAr Calorimeter. (CERN-LHCC-2017-018. ATLAS-TDR-027), Sep 2017.

[19] ATLAS Collaboration. Technical Design Report for the Phase-II Upgrade of the ATLAS Tile Calorimeter. (CERN-LHCC-2017-019. ATLAS-TDR-028), Sep 2017.

[20] ATLAS Collaboration. Technical Design Report: A High-Granularity Timing Detector for the ATLAS Phase-II Upgrade. Jun 2020.

[21] ATLAS Collaboration. Expected performance of the ATLAS detector under different High-Luminosity LHC conditions. Technical Report ATL-PHYS-PUB-2021-023, CERN, Geneva, July 2021.

[22] Technical Proposal for a MIP Timing Detector in the CMS Experiment Phase-2 Upgrade. Technical Report CERN-LHCC-2017-027. LHCC-P-009, 2017.

[23] Matteo Cacciari, Gavin P. Salam, and Gregory Soyez. The anti-k_{t} jet clustering algorithm. *JHEP*, 04:063, 2008.

[24] Matteo Cacciari, Gavin P. Salam, and Gregory Soyez. FastJet user manual. *Eur. Phys. J. C*, 72:1896, 2012.

[25] The Phase-2 Upgrade of the CMS Endcap Calorimeter. Technical Report CERN-LHCC-2017-023. CMS-TDR-019, 2017.

[26] ATLAS Collaboration. Tagging and suppression of pileup jets with the ATLAS detector. ATLAS-CONF-2014-018, 2014.

[27] E. Bols, J. Kieseler, M. Verzetti, M. Stoye, and A. Stakia. Jet flavour classification using DeepJet. *JINST*, 15(12):012, 2020.

[28] ATLAS Collaboration. Measurements of b-jet tagging efficiency with the ATLAS detector using $t\bar{t}$ events at $\sqrt{s} = 13$ TeV. *JHEP*, 08:089, 2018.

[29] ATLAS Collaboration. Expected *b*-tagging Performance with the upgraded ATLAS Inner Tracker Detector at the High-Luminosity LHC. ATL-PHYS-PUB-2020-005, 2020.

[30] CMS Collaboration. Prospects for HH measurements at the HL-LHC. CMS Physics Analysis Summary CMS-PAS-FTR-18-019, 2018.

[31] The LHCb Collaboration. Physics case for an LHCb Upgrade II. Technical Report CERN-LHCC-2018-027, CERN, Geneva, August 2018.

[32] Ilias Efthymiopoulos, Gianluigi Arduini, Vincent Baglin, Helmut Burkhardt, Francesco Cerutti, Serge Claudet, Beniamino Di Girolamo, Riccardo De Maria, Luigi Salvatore Esposito, Nikos Karastathis, Rolf Lindner, Yannis Papaphilippou, Dario Pellegrini, Stefano Redaelli, Stefan Roesler, Francisco Sanchez Galan, Eric Thomas, Andrea Tsinganis, Daniel Wollmann, Guy Wilkinson, and Philip Schwarz. LHCb Upgrades and operation at $10^{34}\,\mathrm{cm}^{-2}\mathrm{s}^{-1}$ luminosity — A first study. Technical Report CERN-ACC-NOTE-2018-0038, May 2018.

[33] J. Albrecht *et al.* Luminosity scenarios for LHCb Upgrade II. Technical Report CERN-LHCb-PUB-2019-001, CERN, Geneva, January 2019.

[34] Laurent Dufour and Jeroen Van Tilburg. Decomposition of simulated detection asymmetries in LHCb. Technical Report LHCb-INT-2018-006. CERN-LHCb-INT-2018-006, CERN, Geneva, Feb 2018.

[35] Riccardo De Maria. Hl-lhc operations with lhcb at high luminosity. presentation EDMS Doc No: 2714414, 2021.

[36] I Efthymiopoulos, S.D. Fartoukh, G Iadarola, N Karastathis, S Papadopoulou, and Y Papaphilippou. Bunch luminosity variations in lhc run 2. In *Proceedings of 12th Int. Particle Acc. Conf. IPAC2021, Campinas, SP, Brazil*, ISBN: 978-3-95450-214-1 ISSN: 2673-5490, pages 4094–4096. JACoW Publishing, 2021.

[37] R. Tomás, I. Efthymiopoulos, and G. Iadarola. Burn-off with asymetric interaction points. In *Proceedings of 12th Int. Particle Acc. Conf. IPAC2021, Campinas, SP, Brazil*, ISBN: 978-3-95450-214-1 ISSN: 2673-5490. JACoW Publishing, 2021.

[38] CMS Collaboration. e-cloud mititation @ hl-lhc. CMS Physics Analysis Summary CMS-PAS-LUM-17-004, 2018.

[39] Xavier Buffat. Stability of the witness bunches. presentation 191st HL-LHC WP2 Meeting, 04.05.2021, 2021.

[40] CMS Collaboration. The Phase-2 Upgrade of the CMS Beam Radiation Instrumentation and Luminosity Detectors. Technical report, CERN, Geneva, July 2021.

[41] Expected performance of the ATLAS detector at the High-Luminosity LHC. Technical report, CERN, Geneva, Jan 2019. All figures including auxiliary figures are available at https://atlas.web.cern.ch/Atlas/GROUPS/PHYSICS/PUBNOTES/ATL-PHYS-PUB-2019-005.

[42] S van der Meer. Calibration of the effective beam height in the ISR. Technical Report CERN-ISR-PO-68-31, 1968.

[43] Luminosity determination in pp collisions at $\sqrt{s} = 13$ TeV using the ATLAS detector at the LHC. Technical report, CERN, Geneva, Jun 2019. All figures including auxiliary figures are available at https://atlas.web.cern.ch/Atlas/GROUPS/PHYSICS/CONFNOTES/ATLAS-CONF-2019-021.

[44] Albert M Sirunyan et al. Precision luminosity measurement in proton-proton collisions at $\sqrt{s} = 13$ TeV in 2015 and 2016 at CMS. *Eur. Phys. J. C*, 81:800, 2021.

[45] CMS Collaboration. CMS luminosity measurement for the 2018 data-taking period at $\sqrt{s}$ = 13 TeV. CMS Physics Analysis Summary CMS-PAS-LUM-18-002, 2019.

[46] A. Babaev et al. Impact of beam-beam effects on absolute luminosity calibrations at the CERN Large Hadron Collider. To be submitted to *Phys. Rev. ST Accel. Beams*., 2021.

[47] Vladislav Balagura. Van der Meer scan luminosity measurement and beam-beam correction. *Eur. Phys. J. C*, 81:26, 2021.

[48] D. Gamba et al. Conceptual specification for the bpms in the HL–LHC era, 2021.

[49] CMS Collaboration. CMS luminosity measurement for the 2017 data-taking period at $\sqrt{s}$ = 13 TeV. CMS Physics Analysis Summary CMS-PAS-LUM-17-004, 2018.

[50] Michael Hostettler, Kajetan Fuchsberger, Giulia Papotti, Yannis Papaphilippou, and Tatiana Pieloni. Luminosity scans for beam diagnostics. *Phys. Rev. Accel. Beams*, 21:102801, 2018.